The mass–metallicity and the fundamental metallicity relation revisited on a fully T_e-based abundance scale for galaxies

Mirko Curti [1,2]⋆ Filippo Mannucci,[3] Giovanni Cresci[3] and Roberto Maiolino[1,2]

[1]*Cavendish Laboratory, University of Cambridge, 19 J. J. Thomson Avenue, Cambridge CB3 0HE, UK*
[2]*Kavli Institute for Cosmology, University of Cambridge, Madingley Road, Cambridge CB3 0HA, UK*
[3]*INAF - Osservatorio Astrofisico di Arcetri, Largo E. Fermi 5, I-50125, Firenze, Italy*

ABSTRACT

The relationships between stellar mass, gas-phase metallicity and star-formation rate (i.e. the mass–metallicity, MZR, and the fundamental metallicity relation, FMR) in the local Universe are revisited by fully anchoring the metallicity determination for SDSS galaxies on the T_e abundance scale defined exploiting the strong-line metallicity calibrations presented by Curti et al. Self-consistent metallicity measurements allow a more unbiased assessment of the scaling relations involving M, Z and SFR, which provide powerful constraints for the chemical evolution models. We parametrize the MZR with a new functional form that allows us to better characterize the turnover mass. The slope and saturation metallicity are in good agreement with previous determinations of the MZR based on the T_e method, while showing significantly lower normalization compared to those based on photoionization models. The Z–SFR dependence at fixed stellar mass is also investigated, being particularly evident for highly star-forming galaxies, where the scatter in metallicity is reduced up to a factor of ∼30 per cent. A new parametrization of the FMR is given by explicitly introducing the SFR dependence of the turnover mass into the MZR. The residual scatter in metallicity for the global galaxy population around the new FMR is 0.054 dex. The new FMR presented in this work represents a useful local benchmark to compare theoretical predictions and observational studies (of both local and high-redshift galaxies) whose metallicity measurements are tied to the abundance scale defined by the T_e method, hence allowing proper assessment of its evolution with cosmic time.

Key words: galaxies: abundances – galaxies: evolution – galaxies: ISM – ISM: abundances.

1 INTRODUCTION

Galaxies continuously undergo chemical evolution, as heavy elements produced in stars are dispersed into the interstellar medium (ISM) and gas flows regulate the level of metal content by diluting its gas phase or directly expelling the enriched gas out of the galactic potential well. The metal content of the gas phase of the ISM (i.e. the *gas metallicity*) is therefore one of the key physical quantities that has to be considered in galaxy evolution studies, as it is strongly sensitive to all the processes that drive and regulate the baryon cycle within galaxies (see Maiolino & Mannucci 2019 for a review on this topic). On global scales, this incessant interplay is naturally reflected by the presence of a number of scaling relations, which encode important information about the evolutionary stages of galaxies.

Among them, the relation between the stellar mass content ($M_\star$) of galaxies and their ISM metallicity (Z), known as the mass–

metallicity relation (MZR, Lequeux et al. 1979), is probably one of the most famous and thoroughly investigated. The advent of the Sloan Digital Sky Survey (SDSS, York et al. 2000) led to a dramatic improvement in the statistics of both stellar mass and metallicity measurements in the local Universe, allowing the assessment of the existence of such a relation with much more significance (e.g. Tremonti et al. 2004). A look to the MZR indubitably reveals how more massive systems appear to be more chemically enriched. This relation holds for a broad range of stellar masses (from ∼10^7 M$_\odot$ to ∼10^{12} M$_\odot$), but its shape changes with varying $M_\star$: the MZR is steep at low masses, then its slope changes in correspondence with a characteristic value of $M_\star$ (the *turnover mass*), asymptotically flattening towards a saturation metallicity. The interpretation of the MZR involves both secular and dynamical processes: on one hand, it may simply imply that massive galaxies represent a more advanced stage of chemical evolution ('chemical downsizing', Somerville & Davé 2015) or, on the other, that they are more capable of retaining metals (thanks to their deeper gravitational potential) compared to low-mass systems, whose enriched gas can be effectively expelled by winds and outflows (e.g. Chisholm et al. 2015). The MZR

has been observed to also hold at redshifts out to 3 and beyond, none the less showing clear signs of evolution (Erb et al. 2006a; Maiolino et al. 2008; Mannucci et al. 2009; Zahid, Kewley & Bresolin 2011; Zahid et al. 2014a; Yabe et al. 2015; Ly et al. 2016; Sanders et al. 2018). In fact, high-z galaxies are observed to be less enriched than local ones for a given stellar mass, an effect that is more predominantly observed at low masses. This evolution can be ascribed to several factors, including an increase in the relative gas content of high-z galaxies (i.e. earlier evolutionary stage or higher dilution by inflows, e.g. Erb et al. 2006b; Lagos et al. 2016), a higher efficiency of gas outflows (e.g. Chisholm, Tremonti & Leitherer 2018) and a reduction in the stellar yields driven by a mass dependence of the IMF (e.g. Lian, Thomas & Maraston 2018). Unveiling the origin, the intrinsic properties of the MZR (i.e. its slope, scatter, turnover mass, normalization) and its redshift evolution are therefore crucial to break the degeneracy on the relative contribution that different physical processes play in driving galaxy evolution.

The scatter in the MZR has been observed to correlate with different galaxy properties. Ellison et al. (2008) first showed an anti-correlation between metallicity and specific star-formation rate for galaxies at a fixed stellar mass. Mannucci et al. (2010) clearly observed a secondary dependence of the MZR on the SFR in a large sample of SDSS galaxies (then extended toward lower masses by Mannucci, Salvaterra & Campisi 2011), with highly star-forming galaxies showing lower metallicities at fixed stellar mass, and first proposed that local galaxies are distributed on a tight surface in 3D space defined by mass, metallicity and SFR. Perhaps even more interestingly, no significant evolution in this scaling relation is seen up to redshift ∼3; therefore, it is often referred to as the 'fundamental metallicity relation' (FMR). Although hotly debated in the literature, the result is generally confirmed when the measurements of all the quantities involved (especially metallicity) are performed self-consistently and the associated observational uncertainties are properly taken into account (see the discussion in Cresci, Mannucci & Curti 2018 and references therein). This suggests that the evolution of galaxies is regulated by smooth secular processes and that an equilibrium condition is set between the involved physical mechanisms over cosmic time.

Many theoretical frameworks have managed to reproduce the observed relation by means of the interplay between the infall of pristine gas, the so-triggered star-formation activity and the amount of enriched material expelled through outflows (e.g. Davé, Finlator & Oppenheimer 2011; Dayal, Ferrara & Dunlop 2013; Lilly et al. 2013; De Rossi et al. 2015; Davé et al. 2017; Torrey et al. 2018). In this context, the redshift evolution of the MZR would naturally arise by sampling different regions of the non-evolving FMR, given the higher average star-formation rate of high-z galaxies. In the context of gas-equilibrium models, the metallicity–SFR dependence is likely the by-product of a more fundamental relationship between the gas metallicity and the gas fraction: this has indeed been observed in small samples of local galaxies (Bothwell et al. 2013, 2016a,b), as well as predicted by cosmological simulations (e.g. Lagos et al. 2016; De Rossi et al. 2017).

This mutual relationship between $M_\star$, metallicity and SFR has been observed and confirmed by several authors (Yates, Kauffmann & Guo 2012; Andrews & Martini 2013; Nakajima & Ouchi 2014; Salim et al. 2014; Grasshorn Gebhardt et al. 2016; Hunt et al. 2016; Hirschauer et al. 2018). However, different prescriptions on the methodology of data analysis, including both the way in which SFR and metallicity are measured and the effects related to different sample selection criteria, have led to the assessment

of M–Z–SFR relations characterized by very different shapes and properties. Furthermore, some recent studies conducted with integral field spectroscopy have suggested that the observed global scaling relations may be driven by more local processes involving the gas metallicity, the stellar mass surface density and the surface density of SFR (Barrera-Ballesteros et al. 2016; Gao et al. 2018; Sánchez Almeida et al. 2018; Sánchez-Menguiano et al. 2019).

The impact of different SFR and metallicity measurements, as well as of the potential biases introduced by sample selection in terms of signal-to-noise cuts, on the overall shape of the FMR has been nicely discussed, for instance, by Telford et al. (2016) and more recently by Cresci et al. (2018). In particular, one of the largest contributions to the differences reported in the literature about the properties of the FMR can be related to the choice of the metallicity diagnostics and calibrations, especially when comparing abundances determined from the T_e method and different methods (i.e. strong-line diagnostics based on predictions from grids of photoionization models), which are well known to be affected by systematic discrepancies (e.g. Kewley & Ellison 2008; López-Sánchez et al. 2012). These may significantly change the strength of the observed dependences, in a way that correlates with all the parameters involved (Yates et al. 2012; Andrews & Martini 2013; Telford et al. 2016). For this reason, when trying to interpret the observations of galaxies in the framework of the FMR predictions, and especially when comparing samples selected at different redshifts, within different environments etc., it is of primary importance to adopt a consistent set of metallicity diagnostics, calibrated on the same abundance scale as those used to derive the benchmark scaling relations.

Although affected by a certain number of weaknesses, mainly attributed to the presence of temperature and chemical inhomogeneities in the nebulae (Peimbert 1967; Stasińska 2002, 2005) and/or to the contribution of diffuse gas to line emission when dealing with global galaxy spectra (Sanders et al. 2017; Zhang et al. 2017), the metallicity measurements based on the T_e method have proven to be in better agreement with independent measurements of stellar metallicities performed in young (i.e. <10 Myr) stars (see e.g. Bresolin et al. 2016; Davies et al. 2017), thus constituting a more reliable absolute scale for chemical abundances compared to that defined by many photoionization models. Adopting the proper abundance scale is indeed crucial to reliably compare observational results with predictions of chemical evolution models and simulations, as many of the observed features in the metallicity scaling relations may change when considering different abundance scales. For example, the very different overall normalization of the MZR, as provided by various metallicity calibrations, largely affects the correct assessment of the asymptotic metallicity, a quantity that has strong implications for the determination of the effective yields of the stellar populations and the capability of galaxies to retain the produced metals.

In this paper we aim at revisiting the M–Z–SFR relations in the local Universe by adopting a set of strong-line diagnostics, presented in Curti et al. (2017), which are self-consistently calibrated on the abundance scale defined by the T_e method over the full range of stellar mass and SFR spanned by SDSS galaxies. This allows us to reduce the possible systematics introduced in the determination of the $M_\star$–Z and SFR–Z dependences by non self-consistent metallicity calibrations. The scaling relations derived in this work will therefore constitute useful benchmarks for forthcoming local studies exploiting metallicity measurements based on the same method, as well as for high-redshift studies aimed at investigating their cosmic evolution.

Table 1. Definition of line ratios adopted throughout this paper.

Notation	Line ratio
R_2	[O II]λ3727, 29/Hβ
R_3	[O III]λ5007/Hβ
N_2	[N II]λ6584/Hα
S_2	[S II]λ6717, 31/Hα
R_{23}	([O II]λ3727, 29 + [O III]λ4959, 5007)/Hβ
O_3O_2	[O III]λ5007/[O II]λ3727, 29
RS_{32}	[O III]λ5007/Hβ + [S II]λ6717, 31/Hα
O_3S_2	[O III]λ5007/Hβ / [S II]λ6717, 31/Hα
O_3N_2	[O III]λ5007/Hβ / [N II]λ6584/Hα

For the purposes of this work, we use strong-line diagnostics to maintain a large statistical significance in all the regions of the parameter space and hence derive more representative properties for the whole galaxy population. Considering only subsamples of individual galaxies with auroral line detections would strongly limit the effective range probed in $M_\star$, SFR and metallicity, while stacked spectra (in bins of $M_\star$ and SFR) would not preserve the statistical information needed to assess the effective role of secondary dependences (e.g. preventing a proper evaluation of the reduction of the scatter in metallicity in different stellar mass bins when accounting for the secondary dependence on SFR). Moreover, adopting a different scheme as in e.g. Curti et al. (2017) (i.e. stacking in bins of [O III]/Hβ versus [O II]/Hβ) would combine galaxies of different stellar mass and SFR, making it impossible to use composite spectra to assess dependences in the latter parameters.

The paper is organized as follows. The sample selection and the methodology used to derive galaxy properties (in particular the gas-phase metallicity) are described in Section 2. In Section 3 we present the analysis of the mass–metallicity relation, while in Section 4 we analyse its dependence on SFR following different approaches and defining a new analytical parametrization for the FMR. Finally, Section 5 summarizes our main results. In Table 1, we report the notations used throughout the paper to indicate the line ratios adopted in our analysis. In this work we adopt a standard ΛCDM cosmology, assuming the parameters presented by Planck Collaboration et al. (2016).

2 SAMPLE SELECTION AND MEASURED QUANTITIES

2.1 Sample selection

Our parent sample is drawn from the seventh data release (DR7) of the Sloan Digital Sky Survey (Abazajian et al. 2009), whose galaxy properties and emission line fluxes are provided by the MPA/JHU catalogue.[1] The criteria followed to define our final sample are described in the following.

We required galaxies to be classified as star forming, according to their position on the [N II]–BPT diagram and following the classification scheme by Kauffmann et al. (2003b). We applied a redshift selection of $z > 0.027$ to ensure the presence of the [O II]λ3727 emission line within the wavelength coverage of the SDSS spectrograph. This allows us to exploit this particular emission line in the metallicity determination while keeping, at the same time, the sample redshift-consistent with that analysed by Curti et al. (2017). However, such a low redshift cut would imply

including galaxies with very small sampling inside the SDSS fibre, as 3 arcsec are equivalent to a projected physical distance of only $\sim$1.6 kpc at $z = 0.027$, thus sampling only the most inner regions. On one hand, this would introduce more uncertainties when applying the aperture corrections for the SFR (see below) and, on the other hand, it would make the metallicity measured within the fibre less representative of the global galaxy metallicity, being more sensitive to the presence of metallicity gradients. To mitigate this problem, we decided to include in our analysis only those galaxies with a covering factor of at least 10 per cent, as inferred from the fraction of the total light that goes into the fibre. In addition, we discarded all galaxies whose catalogue flags indicate unreliable SFR estimates, which also includes all those galaxies showing unphysical aperture correction factors lower than 1.

In terms of signal-to-noise cuts on emission lines, following Mannucci et al. (2010) we have applied an SNR threshold[2] of 15 on the Hα flux only. We do not apply any cut on oxygen, nitrogen and/or sulfur lines, to minimize possible biases in metallicity determination as caused by removing galaxies with low SNR on the emission lines involved in the metallicity diagnostics. In particular, low-metallicity galaxies have low SNR on nitrogen lines, while high-metallicity galaxies have low SNR on oxygen lines. This means that, for instance, introducing an SNR cut on the [O III]λ5007 would translate in removing, in the high-metallicity regime (thus preferentially at high masses), more metal-rich than metal-poor galaxies at fixed stellar mass, in a way that correlates with SFR, hence biasing our determination of the MZR and the M–Z–SFR relation. As an example, it has been shown that an SNR cut on metal lines may contribute to the apparent intersection between the various MZR curves at fixed SFR (see e.g. Yates et al. 2012; Kashino et al. 2016), which could be in principle interpreted as an inversion in the nature of the metallicity–SFR dependence, but that is likely just the consequence of combining selection effects with different SFR and metallicity estimates (Cresci et al. 2018). For a more in-depth discussion on how S/N cuts on different emission lines could introduce biases in the metallicity measurements as a function of different parameters (like $M_\star$ and SFR) in SDSS galaxies, see Telford et al. (2016).

To reliably compute the dust attenuation correction, however, a minimum SNR of 3 on Hβ was also imposed (this removes only an additional 70 galaxies). All emission lines were corrected for reddening from the measured Balmer decrement, assuming the case B recombination (Hα/Hβ = 2.87) and adopting the Cardelli, Clayton & Mathis (1989) extinction law. We then also discarded from the analysed sample all galaxies characterized by extreme extinction, i.e. with values of $E(B - V)$ higher than 0.8.

Finally, we cross-matched DR7 objects with photometric flags from DR12 (which differ from those reported in the DR7 catalogue) and removed galaxies whose photometric flags include DEBLEND_NOPEAK and DEBLEND_AT_EDGE. We also removed galaxies whose stellar mass correction factors are lower than 1, i.e. where the stellar mass derived from the total photometry is lower that the stellar mass derived from the photometry within the fibre. In addition, we have also visually inspected all the objects with $\log(M_\star) < 8.6$ and manually removed the residual poorly deblended systems, which account for another 3 per cent. After

---

[1]Available at http://www.mpa-garching.mpg.de/SDSS/DR7/

[2]Applying the rescaled uncertainties provided by the MPA/JHU group, which include both the uncertainties on the spectrophotometry and continuum subtraction.

applying all these criteria, the total analysed sample is reduced to 153 452 galaxies.

2.2 Stellar mass and star-formation rate

The stellar masses for our sample are provided by the MPA/JHU catalogue and have been estimated from fits to the photometry, following the prescription of Kauffmann et al. (2003a) and Salim et al. (2007). Star-formation rates used in this work are derived from the extinction-corrected H α luminosity inside the fibre, adopting the calibration proposed by Kennicutt & Evans (2012). We then apply the aperture corrections provided by the MPA/JHU catalogue, which build on the work of Salim et al. (2007) to improve those originally provided by Brinchmann et al. (2004), to compute the total SFR for our galaxies. Both stellar masses and SFRs estimates are rescaled to a common Chabrier (2003) inital mass function (IMF).

We choose to adopt the total SFR in our framework, despite the uncertainties potentially introduced by the aperture corrections (e.g. Richards et al. 2016), in order to give a global picture of the mutual relationships between $M_\star$, SFR and metallicity and to facilitate the comparison with studies based on integral field spectroscopy , both in the local and high-redshift Universe. However, the use of fibre-based SFR measurements, despite sampling only the central 3 arcsec of galaxies and thus systematically underestimating the total SFR, is still valuable to characterize the global star-formation activity and investigate trends with other quantities. Moreover, if the metallicity dependence on the SFR is driven by a local dilution effect, being related to the local gas reservoir, linking the metallicity and the SFR measured in the same area (i.e. into the fibre) can be considered more physically meaningful. For this reason, in this paper we present the results of our analysis for both cases, i.e. adopting a total- and a fibre-based SFR. The main differences between the two scenarios will be discussed throughout the paper. Note that Mannucci et al. (2010) adopted fibre SFRs, but applying a much higher redshift cut to the sample (i.e. $z > 0.07$), thus selecting galaxies with a higher coverage fraction within the 3 arcsec fibre.

2.3 Gas-phase metallicity

To measure the metallicity we use a combination of different strong-line diagnostics, assuming the calibrations presented in Curti et al. (2017), which are consistently defined on the T_e-based abundance scale over the entire metallicity range spanned by SDSS galaxies. The full set of metallicity indicators calibrated with this method is presented in Fig. 1. Each calibration has been derived from a set of individual low-metallicity galaxies with auroral line detection together with stacks of high-metallicity galaxies where auroral lines are detected in composite spectra; in this way, the oxygen abundance is self-consistently measured via the T_e method for the entire calibration sample. Compared to the set of diagnostics originally presented in Curti et al. (2017), here we include three additional calibrated line ratios involving sulfur lines: these are in particular S$_2$ ([S II]λ6717, 31/H α), RS$_{32}$ ([O III]λ5007/H β + [S II]λ6717, 31/H α) and O$_3$S$_2$ ([O III]λ5007/H β / [S II]λ6717, 31/H α). The first indicator is similar to the N$_2$ ([N II]λ6584/H α) diagnostic; it saturates at high metallicities but can be useful when dealing with low S/N detections of the [N II]λ6584 emission line or with low-resolution spectra where this line is blended with H α. RS$_{32}$ is instead similar to R$_{23}$ (i.e. [O II]λ3727, 29/H β + [O III]λ5007/H β), given the similar ionization potential of the S$^+$ and O$^+$ ions, but has the advantages of being unaffected by dust extinction and involves a set of emission lines that are more easily observable even in high-z galaxies, as they fall in the main near-infrared bands for a large

range of redshifts. Finally, the latter indicator is similar to O$_3$N$_2$ (i.e. [O III]λ5007/H β / [N II]λ6584/H α), being also similarly unaffected by dust attenuation.

Table 2 summarizes all the coefficients c_n of the polynomial functional forms defining the calibrations presented in Fig. 1; each calibrator is presented in the form $\log(R) = \sum_N c_n x^n$, where R is the considered diagnostic and x is the oxygen abundance normalized to the solar value (Z$_\odot$ = 8.69, Allende Prieto, Lambert & Asplund 2001). The table also reports the root-mean-square (RMS) of the residuals of the fit, which can be assumed as an estimate of the dispersion of the calibrations along the y-axis (i.e. the dispersion in line ratios at fixed metallicity), together with an estimate of the dispersion of the calibration along the x-axis (i.e. dispersion in metallicity at fixed line ratio), labelled as $\sigma_{O/H}$. This latter quantity is estimated comparing the expected metallicity (applying a calibration to the measured line ratio) and the true metallicity (computed with the T_e method) for each point of the calibration sample, and can be assumed as the minimum uncertainty that should be associated with metallicity measurements obtained by using the corresponding diagnostic individually. All the diagnostics proposed in this work have been calibrated against metallicity in the range $12 + \log(O/H) \in [7.6, 8.9]$ and can be safely applied within this range, whereas applications outside this range would rely on extrapolations of the polynomial functions, which may lead to spurious metallicity measurements. For the purpose of this work we use different combinations of diagnostics, according to the availability and SNR of the involved lines, following the scheme presented in Table 3. For sake of clarity, in Fig. 2 we plot each galaxy on the $M_\star$–$\log(O/H)$ plane colour-coded according to the different combination of emission lines involved in its metallicity calculation (upper panel). We also show, within 0.5 dex wide stellar mass bins, the histograms of the metallicity distribution for each galaxy subsample associated with a different set of emission lines (bottom panels). We note that for the vast majority of the sample, both globally and at each fixed stellar mass, it is possible to include all the emission lines (i.e. [O II]λ3727, 29, [O III]λ5007, [N II]λ6584, [S II]λ6717, 31) in the metallicity calculation, as revealed by the predominance of sky-blue points and bars. However, with increasing stellar mass the relative fraction of galaxies whose metallicity has been inferred from a different combination of lines increases, as a primary consequence of the [O III]λ5007 line falling below the detection threshold.

Using multiple diagnostics at the same time is crucial to break the degeneracies affecting the calibrations of double-branched indicators and to exploit the information provided by multiple emission lines, whose (both direct and indirect) dependence on O/H can vary in different metallicity ranges, hence setting tighter constraints on the final abundance measurement. Nevertheless, in our procedure we avoid using double-branched diagnostics when their calibrations approach the region of the 'plateau', hence always choosing the best possible combination of independent and monotonic metallicity indicators. In practice, this translates to avoiding the use of R$_3$ when $\log(R_3) > 0.5$ and R$_2$ when $\log(R_2) > 0.45$, encoding the information from those emission lines only within other diagnostics (like O$_3$O$_2$ or O$_3$N$_2$). However, this criterion affects overall only a small number of galaxies, preferentially at low $M_\star$.

The metallicity of each galaxy in the sample is computed by searching for the value that minimizes the chi-square defined simultaneously by the selected diagnostics as:

$$\chi^2 = \sum_i \frac{(R_{\mathrm{obs}_i} - R_{\mathrm{cal},i})^2}{\sigma_{\mathrm{obs}}^2 + \sigma_{R_{\mathrm{cal},i}}^2}, \tag{1}$$
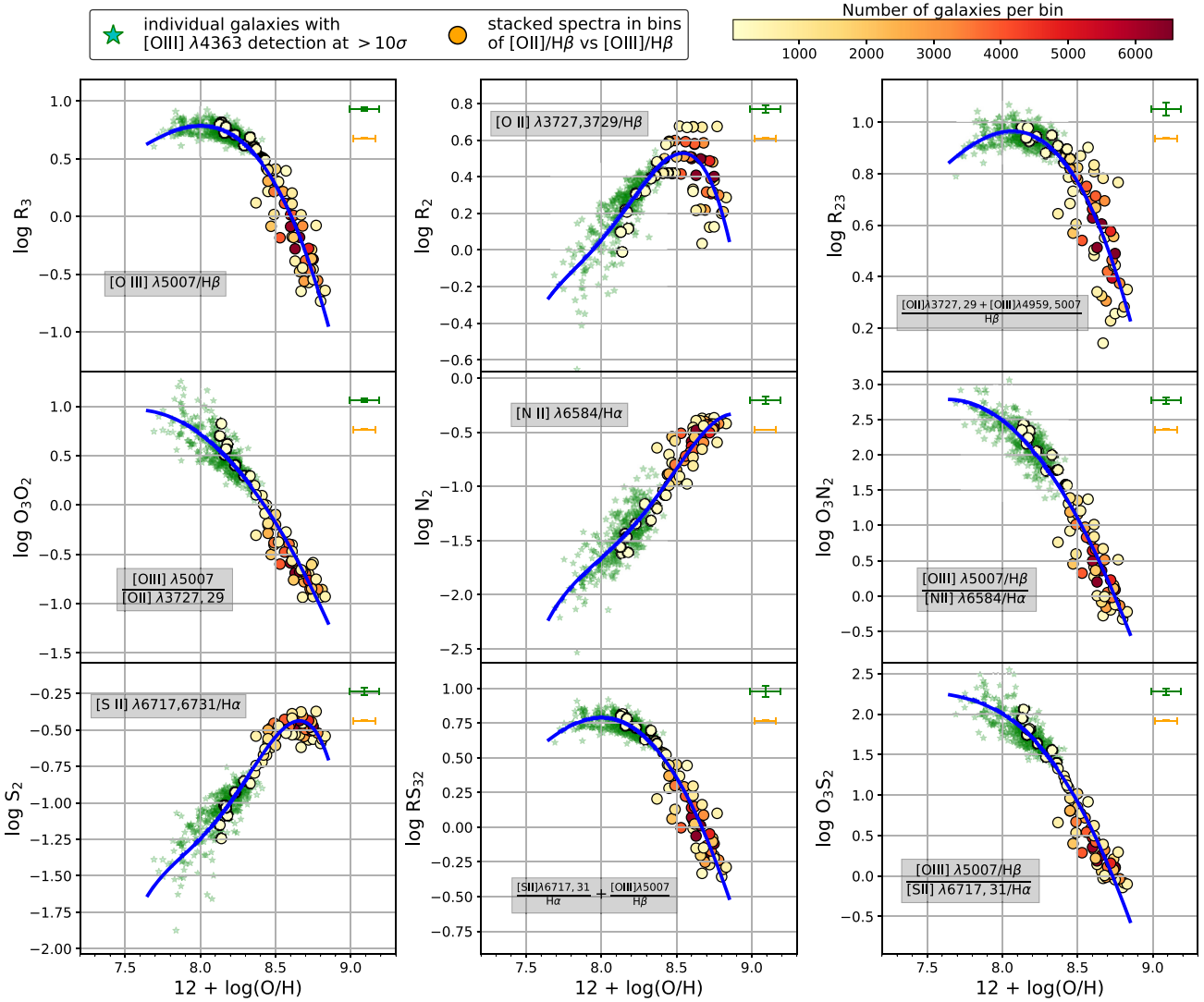
Figure 1. The set of strong-line metallicity diagnostics used in this work. All of them have been calibrated from T_e-based measurements of oxygen abundance in a combined sample of individual galaxies (small green stars) and stacked spectra (circular points, colour-coded by the number of galaxies per stack) in bins of $\log([O\,\textsc{ii}]/H\beta) - \log([O\,\textsc{iii}]/H\beta)$) (see Curti et al. 2017 for details of the stacking procedure and analysis). The blue curves represent the polynomial fit that defines the calibration for each diagnostic.

Table 2. Best-fitting coefficients of the polynomial functions ($\log(R) = \sum_N c_n x^n$, with $x = Z - 8.69$) defining the metallicity calibrations presented in Fig. 1. The RMS column reports the root-mean-square of the fit for each calibrator, while σ represents an estimate of the dispersion of the calibration along the metallicity axis.

Diagnostic	c_0	c_1	c_2	c_3	c_4	c_5	RMS	σ
R_2	0.435	−1.362	−5.655	−4.851	−0.478	0.736	0.11	0.10
R_3	−0.277	−3.549	−3.593	−0.981			0.09	0.07
O_3O_2	−0.691	−2.944	−1.308				0.15	0.14
R_{23}	0.527	−1.569	−1.652	−0.421			0.06	0.12
N_2	−0.489	1.513	−2.554	−5.293	−2.867		0.16	0.10
O_3N_2	0.281	−4.765	−2.268				0.21	0.09
S_2	−0.442	−0.360	−6.271	−8.339	−3.559		0.11	0.06
RS_{32}	−0.054	−2.546	−1.970	0.082	0.222		0.07	0.08
O_3S_2	0.191	−4.292	−2.538	0.053	0.332		0.17	0.11

Table 3. Combination of metallicity diagnostics adopted in this work. Composite diagnostics (in parenthesis) are only used when individual diagnostics approach their saturation values, e.g. for $\log(R_3) > 0.5$ and/or $\log(R_2) > 0.45$.

Lines detected at $\geq 3\sigma$	Diagnostics used	# galaxies
[O III], [O II], [N II], [S II]	R_3, R_2, N_2, S_2, (O_3N_2,O_3O_2)	115 005
[O III], [N II], [S II]	R_3, N_2, S_2, (O_3N_2,O_3S_2)	5292
[O II], [N II], [S II]	R_2, N_2, S_2	14 917
[O III], [O II], [S II]	R_3, R_2, S_2, (O_3S_2)	108
[O III], [O II], [N II]	R_3, R_2, N_2, (O_3N_2)	1853
[N II], [S II]	N_2, S_2	14 547
[O II], [O III]	R_2, R_3, (O_3O_2)	8
[O III], [N II]	R_3, N_2, (O_3N_2)	502

where R_{obs_i} are the observed line ratios while $R_{\mathrm{cal},i}$ are the values predicted by the calibration for a given metallicity. Both the uncertainty on the observed line ratio σ_{obs} and the intrinsic dispersion of calibration $\sigma_{R_{\mathrm{cal},i}}$ are taken into account in the procedure. A Monte Carlo Markov chain (MCMC) is run, varying line fluxes according to a Gaussian distribution centred on the measured line ratio and σ equal to the measurement error, and the chi-square is minimized at each step to generate a log(O/H) distribution. All line ratios have been preliminarily corrected for reddening (assuming the case B recombination and the Cardelli et al. 1989 law), so extinction is not a free parameter in the procedure. However, the error on the reddening correction is propagated on the uncertainty of each observed line ratio. From the generated log(O/H) distribution, the median value is assumed as the inferred metallicity while the 1σ interval (computed from the 16th and 84th percentiles) is adopted as an estimate of the associated uncertainties. We discarded galaxies whose uncertainty on the final metallicity exceeded 0.3 dex; therefore, the final number of galaxies with robust oxygen abundance determination is 151 862.

A very important consideration that we want to stress here is that the main results presented throughout the paper are robust against the choice of different combinations of line ratios, as proven also by the good internal consistency of the proposed calibrations (see figs 10 and 11 of Curti et al. 2017). None the less, some slight differences in the metallicity determination may arise due to small systematics between the nitrogen-based and oxygen-based diagnostics, with [N II]λ6584-based diagnostics preferentially underestimating metallicity compared to purely oxygen-based ones, especially in the low-metallicity regime (where the calibrations are less constrained and more uncertain due to the smaller statistics). However, this does not significantly affect or hide in any manner the presence of trends between $M_\star$, metallicity and SFR, although it can change the strength of their mutual dependences (see also the discussions in Sections 3.2 and 4.2). For this reason, in Appendix B we present and discuss the differences between the MZR and M–Z–SFR relations derived adopting only nitrogen- and only oxygen-based metallicity calibrations respectively. The simultaneous use of multiple diagnostics is indeed aimed at minimizing the impact of these potential systematics.

3 THE MASS–METALLICITY RELATION

3.1 A new parametrization for the MZR

We study here the distribution of our galaxy sample in the $M_\star$ versus log(O/H) plane, i.e. the mass–metallicity relation (MZR). In order
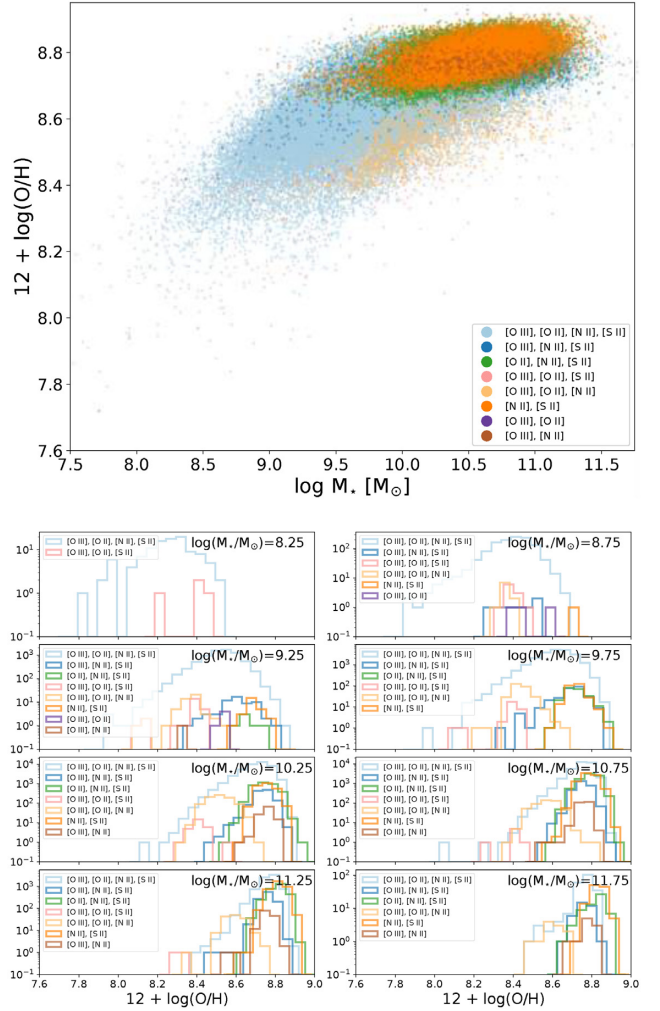
Figure 2. *Upper panel:* Distribution of galaxies in our sample on the stellar mass–metallicity plane. Each galaxy on the plot is colour-coded according to the different combination of emission lines involved in its metallicity calculation, following the scheme presented in Table 3. *Bottom panels:* Histograms (in log-scale) of the metallicity distribution, within $M_\star$ bins of 0.5 dex, for each of the subsamples whose metallicity has been derived adopting a different set of emission lines.

to derive the representative properties of this scaling relation, we sort the sample in 0.15 dex wide stellar mass bins and compute the median and standard deviation of the metallicity distribution in each bin; we limit the analysis only to $M_\star$ bins including at least 25 galaxies, i.e. for $7.95 < \log(M_\star) < 11.85$, in order to maintain a meaningful statistical representation.

The *median* MZR is then parametrized with the following functional form:

$$12 + \log(\mathrm{O/H}) = Z_0 - \gamma/\beta * \log\left(1 + \left(\frac{M}{M_0}\right)^{-\beta}\right). \quad (2)$$

In this equation, Z_0 is the metallicity at which the relation saturates, quantifying the asymptotic upper metallicity limit, while M_0 is the characteristic turnover mass above which the metallicity asymptotically approaches the upper metallicity limit, Z_0. At stellar masses $M_\star < M_0$, the MZR reduces to a power law of index γ. Compared to previous works (e.g. Moustakas et al. 2011; Zahid et al. 2014a), the presence of the β parameter allows us to better control the width of

Table 4 Best-fitting values for the parameters of the MZR derived with the new set of T_e-based calibrations of Fig. 1 on the SDSS galaxy sample. The upper row assumes the new parametrization of equation (2) proposed in this work. The bottom row assumes instead a modified version of the parametrization proposed by Zahid et al. (2014b), as given by equation (3).

	Z_0	$\log(M_0/M_\odot)$	γ	β
Equation (2)	8.793 ± 0.005	10.02 ± 0.09	0.28 ± 0.02	1.2 ± 0.2
Equation (3)	8.792 ± 0.003	10.26 ± 0.06	0.38 ± 0.08	–

the transition region between the two extremes, providing a better constraint on the turnover mass and overall a better fit to our median points. In other words, β quantifies how 'fast' the curve approaches its saturation value: the smaller the value of β, the broader the knee, and vice versa. We perform a robust fit of our median MZR relation adopting the the above functional form and using the PYTHON-based LMFIT package (Newville et al. 2014). The data are weighted in the fit according to the metallicity dispersion and the number of objects in each individual $M_\star$ bin and the errors on the parameters are estimated from the 1σ confidence levels based on an MCMC simulation. The best-fitting parameters with the associated errors are given in Table 4. The scatter of individual galaxies around the best-fitting relation is 0.07 dex, somewhat lower than in previous determinations (which found a scatter around ∼0.1 dex, e.g. Tremonti et al. 2004).

The upper panel of Fig. 3 shows our new strong-line MZR: small grey points are individual galaxies, while grey filled contours encompass the 68 per cent, 84 per cent, 95 per cent and 99 per cent of the galaxy distribution in the $\log(M_\star)$–$\log(O/H)$ plane. White points are the median metallicities in 0.15 dex stellar mass bins (with black error bars marking the metallicity dispersion in each bin), while the red curve represents the best-fitting *median* MZR according to the functional form of equation (2). The assumed value for solar abundance (8.69 ± 0.05, Allende Prieto et al. 2001) is marked by the horizontal orange stripe. Our best-fitting median MZR asymptotes at $12 + \log(O/H) = 8.793 \pm 0.005$ (i.e. ∼1.27 times the solar abundance) presents a turnover at $\log(M_\star/M_\odot) = 10.02 \pm 0.09$ and is characterized by a low-mass-end slope of $\gamma = 0.28 \pm 0.02$. Different functional forms still provide a good representation of the data, although the best-fitting values of the parameters can be different. In particular, adopting a slightly modified version of the Zahid et al. (2014a) functional form (by substituting the exponential term inside the 10-base logarithm in their equation (5) with a power of ten), i.e.

$$12 + \log(O/H) = Z_0 + \log(1 - 10^{-\left(\frac{M}{M_0}\right)^\gamma}), \qquad (3)$$

we obtain a slightly higher value for the turnover mass (10.26 ± 0.06), but a steeper low-mass-end slope (0.38 ± 0.09), simply due to the absence of the β parameter, which causes the width of the knee to be fixed to a much larger value, allowing the purely linear part of the relation to occur at very low masses, largely outside the effective sampled mass range. However, in the range of stellar masses probed by our sample, the two representations are almost identical. The best-fit parameters assuming the MZR representation of equation (3) are also given in Table 4.

### 3.2 Comparison with different MZRs from the literature

The bottom panel of Fig. 3 presents a comparison between our best-fitting MZR and previous estimates of the MZR from the literature, based on different methods for metallicity determination. The grey

shaded areas here mark the 1 and 2σ deviations from the median values in each $M_\star$ bin. All the mass–metallicity relations shown in this plot have been re-derived by applying the different methods and metallicity calibrations adopted in each reference work to the sample considered in this work, in order to minimize the systematics induced by different sample selection criteria. Additional cuts in signal-to-noise (i.e. at SNR = 3) on different emission lines are implemented when required by the relative calibration method. In particular, the metallicities derived with the method described in Tremonti et al. (2004) are already provided in the MPA/JHU catalogue. The Kewley & Dopita (2002) relation is based on the recursive technique (involving R_{23}, O_3O_2 and N_2O_2) presented in their paper and then revised by Kobulnicky & Kewley (2004), while the Mannucci et al. (2010) MZR is based on the R_{23} and N_2 semi-empirical calibrations presented in Maiolino et al. (2008). Similarly to Tremonti et al. (2004), the calibrations adopted in the latter works provide oxygen abundances based on the predictions of different grids of photoionization models. More precisely, for the Maiolino et al. (2008) calibrations this is true only for $12 + \log(O/H) > 8.4$, while in the low-metallicity regime they are based on a sample of galaxies with T_e measurements. The Pettini & Pagel (2004) curve is instead derived by means of their O_3N_2 calibration, which is built on T_e metallicity measurements in individual H II regions. Finally, the Andrews & Martini (2013) and Yates et al. (2019) curves are directly taken from the literature, as they are based on very different samples and/or techniques. Specifically, Andrews & Martini (2013) provide a T_e-based version of the MZR by measuring the electron temperatures (and hence the metallicities) from SDSS stacked spectra in bins of stellar mass, whereas Yates et al. (2019) adopt a revised version of the T_e method on a complied sample of galaxies (both from the literature and from the MANGA survey) with auroral line detections.

In addition, we plot the oxygen abundance measurements derived for nearby galaxies in the local Universe (including the Milky Way), which exploits stellar spectroscopy of young (∼10–50 Myr) red and blue supergiants (RSG, BSG) to probe the chemical enrichment level (Gazak et al. 2015; Davies et al. 2015; Bresolin et al. 2016; Kudritzki et al. 2016); the data points are taken from the compilation presented in table 3 of Davies et al. (2017, see also references therein). Metallicity measurements from blue supergiants are plotted as blue crosses, while abundances measured from red supergiants are plotted as red stars; a few galaxies in the sample have both measurements, which always agree within 0.1 dex. These measurements trace the abundances of the ISM with an independent approach compared to studies targeting H II regions, but are sensitive to a similar time-scale of chemical enrichment.

The abundances probed by means of BSG and RSG spectroscopy are in better agreement with the curves based on T_e metallicity measurements rather than with the theoretical derivations the MZR, perfectly matching the normalization of our new MZR at high masses, but slightly deviating at lower masses. At $\log(M_\star)$ lower than 9.5, they are systematically offset towards lower abundances compared to our median values, although still in agreement within 2σ considering the large scatter of the galaxy distribution in the $M_\star$–O/H plane in the low-mass–low-metallicity regime. It is also worth noting here that the stellar metallicity is mainly traced by the abundance of iron-peak elements, while the metallicity of the gas phase of the ISM is traced by the oxygen abundance (and more rarely by other α-elements); therefore, different α/Fe ratios might contribute to the observed discrepancy.

Our median MZR presents considerable differences in slope and normalization, as expected, from those derived with theoretical
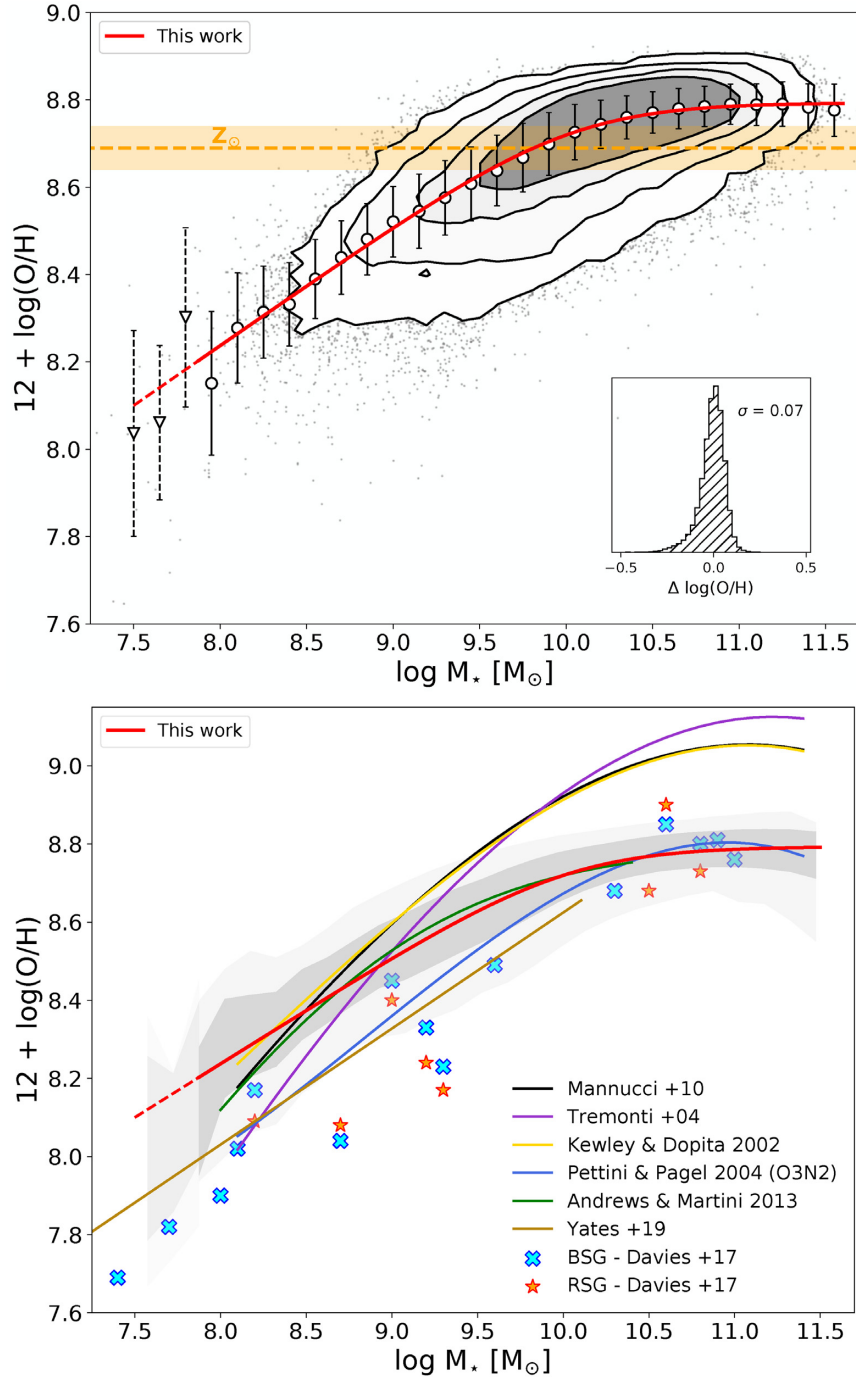
Figure 3. *Upper panel*: Mass–metallicity relation (MZR) for the sample of SDSS galaxies analysed in this work, as derived by the set of metallicity calibrations presented in Fig. 1. Grey points represent individual galaxies, while the filled regions encompass the 1, 2, 3 and 4σ levels of the density contours of the distribution in the log($M_\star$)–log(O/H) plane. White circles (and associated error bars) are median metallicities (and dispersions) in narrow 0.15 dex bins of stellar mass, while the solid red curve represents the best fit to those median points according to the MZR parametrization given in equation (2). The dashed red part instead is the extrapolation of the MZR fit in the low-mass regime, with the low-mass bins (i.e. with fewer than 25 objects) represented by white triangles with dashed error bars. The dashed orange band marks the value assumed for the solar abundance (i.e. $Z_\odot = 8.69 \pm 0.05$, Allende Prieto et al. 2001). The small box in the lower right-hand part of the figure show the distribution of the metallicity dispersion of the individual galaxies around the best-fitting MZR, whose 1σ dispersion is equal to 0.07 dex. *Bottom panel*: Comparison between the MZR derived in this work (red curve, with grey areas encompassing the 1σ and 2σ dispersions in each log($M_\star$) bin) and different predictions of the MZR from previous studies in the literature, colour-coded as reported in the legend. Strong-line MZRs have been re-derived by applying each different calibration method to our sample. In particular, the Kewley & Dopita (2002), Tremonti et al. (2004), Mannucci et al. (2010) curves are anchored to an abundance scale defined by different grids of photoionization models, while the Andrews & Martini (2013), Pettini & Pagel (2004) and Yates et al. (2019) curves are based on the T_e-based abundance scale. Red stars and blue crosses represent the abundances derived in nearby galaxies from stellar spectroscopy of red and blue supergiants respectively, as collected by Davies et al. (2017).
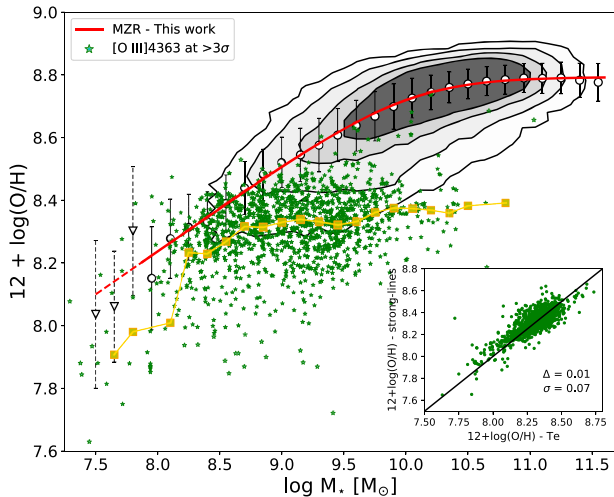
Figure 4. The positions of galaxies with [O III]λ4363 detection above 3σ (with derived T_e-based metallicities) are plotted on the mass–metallicity plane and compared with the full distribution of SDSS galaxies (based on strong-line metallicities) and our new median MZR (symbols and colours are as in Fig. 3). The median metallicity in bins of $M_\star$ for the [O III]λ4363 galaxies is marked by yellow squares. At fixed stellar mass, requiring an [O III]λ4363 detection preferentially selects the most metal-poor galaxies, potentially biasing the assessment of the MZR. In the small inner box, we compare the T_e-based and the strong-line-based metallicities for these galaxies. They show good consistency, with an offset and a dispersion from the 1:1 relation of 0.01 and 0.07 dex respectively.

strong-line calibrations, especially for what concerns the normalization of the high-mass regime and the saturation metallicity. This is easily explained considering the discrepancy between the abundance scale defined by the T_e method and that adopted by the photoionization models that are at the base of the respective strong-line calibrations. Overall, the agreement of our best-fitting median MZR with that from Andrews & Martini (2013) is instead quite remarkable over the entire range of stellar masses. The two relations only slightly deviate between $7.95 < \log(M_\star) < 8.5$, with our MZR characterized by a shallower slope. This leads to a divergence in the prediction of the two relations when relying on their extrapolations at lower masses. A possible explanation resides in the fact that the oxygen abundance inferred from stacked spectra (as in Andrews & Martini 2013) is a weighted average on the intensity of the auroral lines, which might bias low the metallicity determination in the $M_\star$ stacks at low masses, where the number of galaxies per bin strongly decreases.

More recently, Yates et al. (2019) derived the MZR for a sample of 118 local, intermediate and low-mass (i.e. $M_\star \lesssim 10^{10}\,\mathrm{M_\odot}$) galaxies, exploiting a revised version of the classical T_e method; their MZR is characterized by a lower normalization (on average ~0.2 dex in the overlapping $M_\star$ range) compared to the MZR presented in this work. One possible explanation is based on the bias introduced by the requirement of an [O III]λ4363 detection, and can be easily tested within the SDSS sample. Not surprisingly indeed, the galaxies in the SDSS-DR7 with [O III]λ4363 detection (i.e. those objects for which it is possible to derive T_e metallicities) all belong to the large scattered region below the median MZR at low stellar masses (i.e. below $\log(M_\star) = 10$). This is due to the fact that, at fixed stellar mass, it is easier to detect the [O III]λ4363 line in low-metallicity galaxies. This is shown in Fig. 4, where the positions of galaxies with [O III]λ4363 detection above 3σ are plotted on the mass–metallicity

plane and compared with the 5σ-level density contours of the full SDSS galaxies distribution and the new median MZR derived in this section, clearly demonstrating how biased the SDSS MZR could be when selecting exclusively these objects. The oxygen abundance for these galaxies is calculated following the scheme described in Curti et al. (2017), for consistency with the method implemented in the calibrations of the metallicity diagnostics; in particular, the [O III]λ4363 emission line is exploited to compute the electron temperature of the O^{++} zone (t_3), while the ff-relations are adopted to infer the flux of the [O II]λ7320, 7330 auroral line and derive the temperature of the O^+ zone (t_2). We also check that the strong-line metallicity scheme adopted in this work is not introducing any clear systematics in the abundance determination for these galaxies by showing, in the small inner box within Fig. 4, that the T_e-based and strong-line-based metallicities for such objects are fully consistent, with an average offset of only 0.01 dex and a scatter of 0.07 dex. This is not surprising, as many of these galaxies belong to the sample exploited in the calibration of the diagnostics presented in Curti et al. (2017) and Fig. 1. It is also worth noting here that this is the region where the effects of the FMR are known to be more prominent (see e.g. Section 4.1), hence where the analysis of galaxy samples characterized by different average SFRs can produce MZR with different slopes. This effect, combined with small statistics and the requirement of strong [O III]λ4363 detections (which preferentially selects among the most metal-poor galaxies at fixed $M_\star$ and SFR) might explain the offset observed between the MZR derived in this work and the one presented by Yates et al. (2019).

The slope of the MZR is also sensitive to other types of selection effects. For example, because the SDSS sample is apparent magnitude limited, increasing the minimum redshift threshold removes a larger fraction of low-mass galaxies than high-mass galaxies and, at the same time, increases the average SFR of the sample in the low-mass regime. This causes a decrease of the mean metallicity at fixed stellar mass (due to the effect of the FMR) and therefore a steepening in the low-mass-end slope of the MZR. Modifying the threshold in H α SNR also produces similar effects. None the less, sample selection effects might be not enough to fully explain the observed discrepancy, as systematics between the different methods (modified T_e method versus strong-line calibrations) might be present and will be subject to further investigation.

As mentioned at the beginning of Section 3.1, we have so far considered in our analysis only stellar mass bins with more than 25 objects, which correspond to $\log(M_\star) > 7.95$. Therefore, the best-fitting MZR discussed so far has to be considered trustworthy only in the $7.95 < \log(M_\star) < 11.85$ range, whereas extrapolation outside this range is unsafe and can bring to spurious results. Below this threshold, in fact, when entering the low-mass regime, the poor statistics prevents a robust determination of the properties of the MZR. An additional big issue is related to the intrinsic uncertainties associated with the stellar mass measurements itself. As the specific star-formation rate increases, the relative contribution from the old stellar population (which makes most of the stellar mass) to the total light in the z-band can be ≪1 per cent, hence largely affecting the accuracy of the $M_\star$ determination in these galaxies. This effect is likely to be more prominent at low masses, where the contamination of spurious high-mass objects can have a bigger impact on the assessment of the statistical properties of the population.

However, we try to extend the analysis presented above to the low-mass end by removing the threshold of 25 objects per bin in this regime, hence computing median metallicities down to $\log(M_\star) = 7.5$. This means that the lowest-mass bins are now populated by fewer than 10 objects. These points are shown as
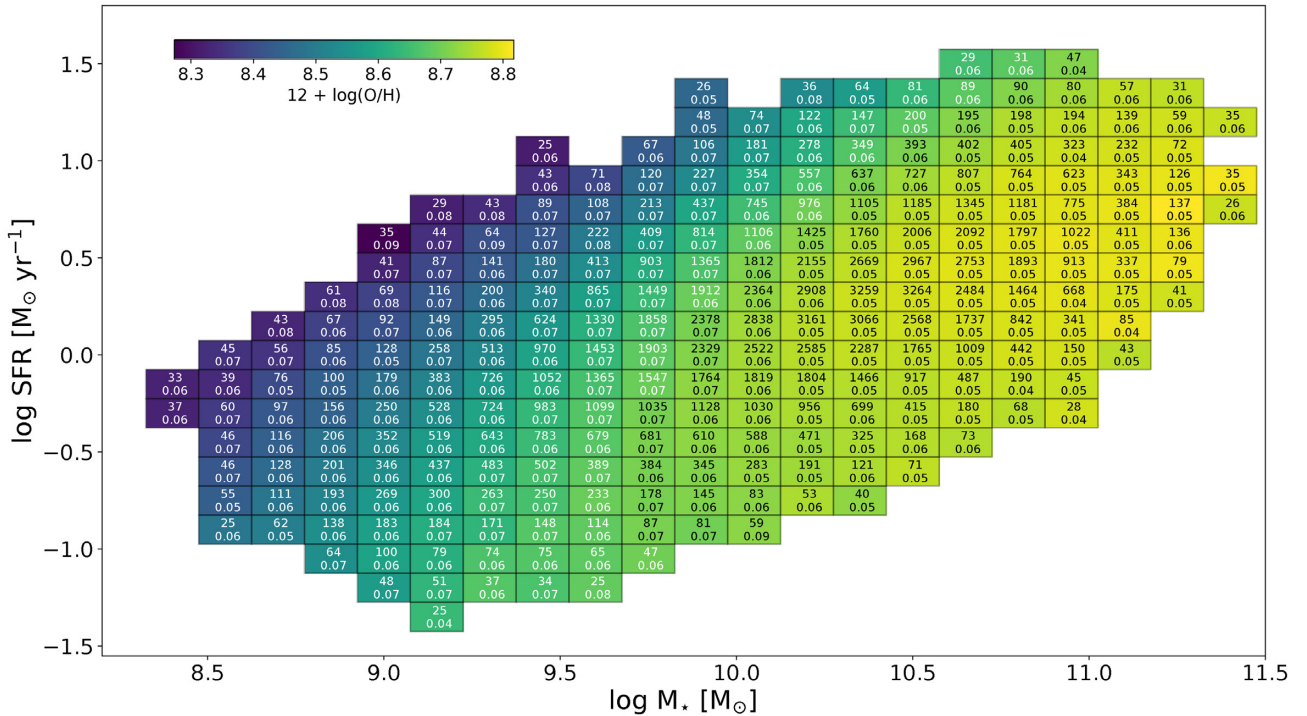
Figure 5. The binning scheme exploited in this work to investigate the $M_\star$–Z–SFR relation. Each 0.15 dex wide bin in $M_\star$ and SFR is colour-coded by its median metallicity, while the number of galaxies and the internal metallicity dispersion are reported for each of them. Only those bins including more than 25 galaxies are considered in this analysis.

triangles (with dashed error bars) in the upper panel of Fig. 3, while the extrapolation of the best-fitting MZR is shown by the dashed red line. The extrapolation produces a slight overestimate of the metallicity compared to the median points at the lowest masses, although being fully consistent within 1σ; including these points in the MZR fitting procedure does not strongly affect the overall shape of the relation, producing only a small steepening of the low-mass-end slope (up to $\gamma = 0.29$).

We finally note that, as already mentioned in Section 2.3, small systematics are present between nitrogen-based and oxygen-based diagnostics within our strong-line calibration set, especially at low metallicities (hence preferentially at low masses). Given the poor sampling of this region of the mass–metallicity plane, this is where such effects can have a larger impact on the determination of the slope of the MZR. To have an estimate of the amplitude of this effect, we refer the reader to the analysis presented in Appendix B.

4 THE FUNDAMENTAL METALLICITY RELATION

4.1 The correlation between $M_\star$, Z and SFR

We now want to consider the mutual relations between stellar mass, metallicity and star-formation rate, the M–Z–SFR relation. First, we explore the dependence of the MZR on the total SFR. To do so, we sorted the sample into 0.15 dex bins of stellar mass and 0.15 dex in total SFR and computed the median metallicity (and dispersion) in each bin. As in the previous section, we limit the analysis only to those bins including at least 25 galaxies, to sample as much as possible the low-mass–high-SFR regime while keeping a reasonable statistics inside each bin at the same time.

Fig. 5 shows our binning grid in the $M_\star$–SFR plane: each bin is colour-coded by its median metallicity, while the metallicity dispersion and the number of objects within each bin is reported within. The upper left-hand panel of Fig. 6 shows instead different mass–metallicity relations at fixed SFR (colour-coded for their total SFR values). The fit to the (global) median MZR (presented in Section 3.1) is shown in black, while grey contours trace the 1σ metallicity dispersion in each mass bin. A clear segregation in SFR is visible, with highly star-forming galaxies characterized by lower metallicities compared to low star-forming galaxies of the same stellar mass. Fig. 6 also reveals that the tightness of the observed secondary dependence of the MZR on the SFR strongly decreases in the high-mass regime (i.e. above $\log(M_\star) \gtrsim 10$), with all the different MZRs flattening towards the same saturation value Z_0. We can easily visualize this trend by directly tracing the metallicity dependence on SFR at fixed stellar mass (top right-hand panel of Fig. 6). Lines of constant stellar mass flatten with increasing $M_\star$, with the dependence of metallicity on SFR strongly weakening for curves corresponding to $\log(M_\star) \gtrsim 10.5$ M$_\odot$. The strength of the Z–SFR dependence is also a function of the SFR itself and becomes stronger at high SFRs, as can be seen from the clear steepening of the different curves in the high-SFR regime at almost all stellar masses.

It is also interesting to investigate the mutual relationship between $M_\star$, metallicity and specific star-formation rate (sSFR = SFR/$M_\star$, bottom panels of Fig. 6), which describes the relative weight of recent star formation over the global star-formation history of a galaxy. At low masses, the dependence is present over the entire sSFR range, while weakening for increasing masses at sSFR < $10^{-9.5}$ yr^{-1}, until almost completely disappearing for the highest-mass bins. However, when describing the relation in terms of sSFR, the change in slope of the Z–sSFR anti-correlation become increasingly evident in the high-sSFR regime (i.e. for sSFR $\gtrsim 10^{-9.5}$
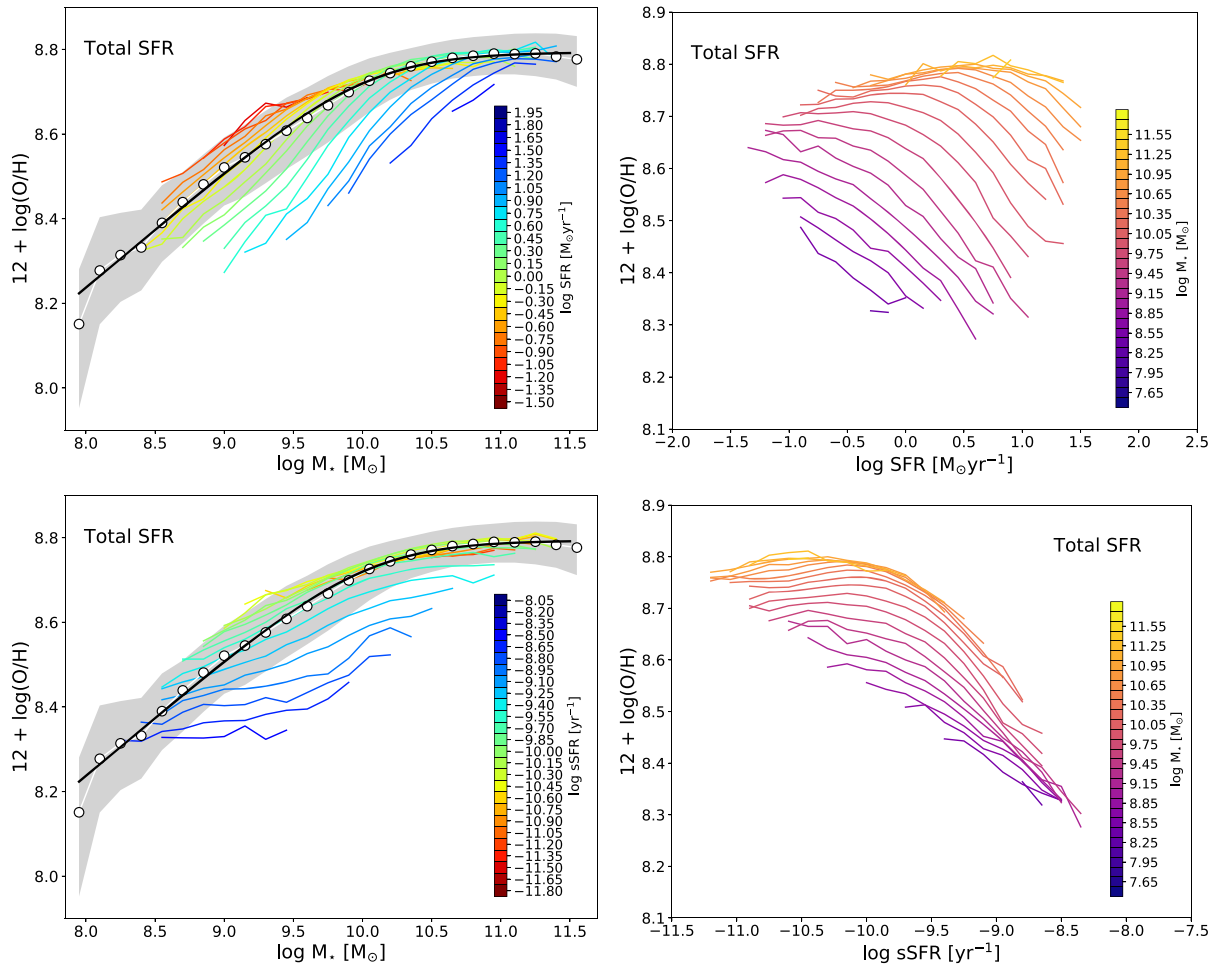
Figure 6. *Upper panels*: M–Z–SFR relation for our sample. Different median MZRs in (0.15 dex wide) bins of total SFR are plotted in the left-hand panel, highlighting the secondary dependence of the mass–metallicity relation on the SFR, especially at low masses and high star-formation rates. In the right-hand panel, the relation between log(O/H) and SFR is plotted for different bins of stellar mass. *Bottom panels*: Same as above, assuming the sSFR = SFR/$M_\star$ as the third variable.

yr^{-1}, which comprises ∼16 per cent of the entire sample) at almost any stellar mass. These plots confirm the trend originally found by Mannucci et al. (2010) and suggest that a proper description of M–Z–SFR relationships should allow for non-linear trends with (s)SFR, as also previously suggested by other studies (e.g. Salim et al. 2014) using different metallicity calibrations than the ones used in this work.

A close inspection of Fig. 6 reveals a slight intersection of the different MZR curves at high masses and low SFR or, equivalently, that there is an inversion in the trend of O/H versus SFR curves at fixed high stellar masses. This effect has been already reported before, although much more prominently as e.g. in Yates et al. (2012), as mainly driven in that case by different SFR measurements and the use of Tremonti et al. (2004) metallicities (see the discussion in Cresci et al. 2018). In our specific case, however, a possible explanation is related to considering total SFRs rather than fibre SFRs in our analysis. In fact, when applying aperture corrections to fibre SFRs, metallicity and stellar masses stay unchanged, while we associate the same galaxy with a higher total-SFR bin. Since the aperture correction factor correlates with fibre SFR and, at fixed stellar mass, fibre SFR correlates with metallicity (as an effect of the FMR), the relative fraction of galaxies that change

SFR bin in the high-mass–low-fibre SFR region is preferentially constituted by the most metal-rich galaxies in those bins. This has the effect of lowering the median metallicity in high-$M_\star$–low-total-SFR bins while increasing it in high-$M_\star$–high-total-SFR bins, compared to the analysis conducted on fibre-based SFR. Another possible explanation is related to the impact of metallicity gradients at high $M_\star$, where they are generally steeper (Belfiore et al. 2017), which would make the central fibre metallicity less representative of the global metallicity of the galaxy and therefore the comparison with the total SFR less fair. Finally, the uncertainties associated with the derivation of aperture corrections introduce spurious noise in our relationships. Indeed, when considering SFRs measured within the fibre (as shown in Fig. 7), the inverted trends fully disappear, and the O/H versus SFR curves at high masses are flat, as expected (i.e. no clear secondary dependence of the MZR on SFR at high masses). Recently, Vale Asari et al. (2019) suggested that removing the contamination by diffuse ionized gas (DIG) from the SFR and O/H measurement (in particular when adopting the N_2 diagnostic) might reveal the presence of such an inversion at high $M_\star$ even for fibre-based star-formation rates. In our case, the magnitude of such an effect is none the less small enough to not affect any of the subsequent analysis.
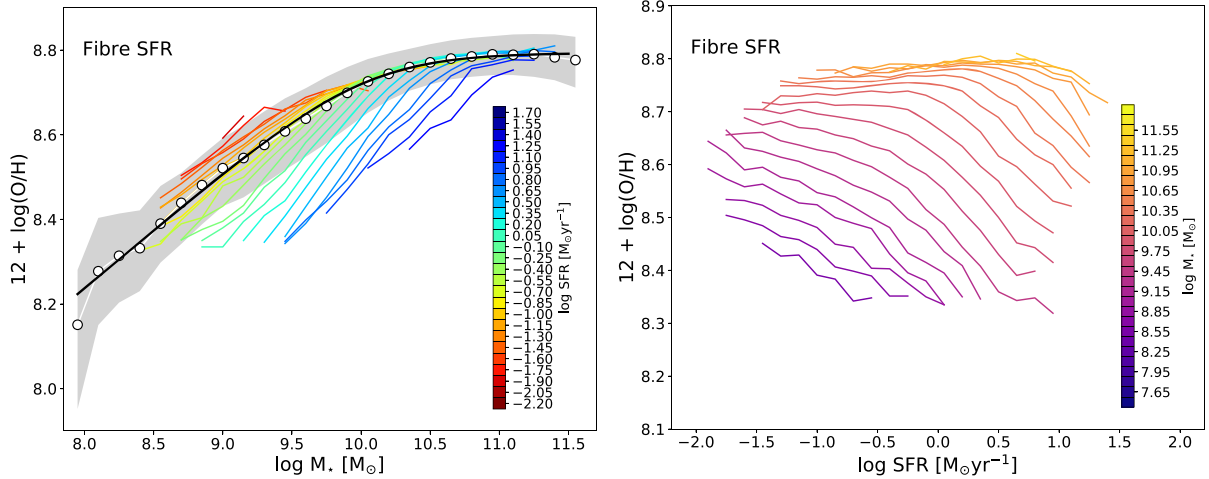
Figure 7. Same as upper panels of Fig. 6 for fibre-based SFRs.

Following the prescriptions by Salim et al. (2014), we can also visualize the dependence of metallicity on SFR at fixed stellar mass assuming a non-parametric approach. In more detail, Salim et al. (2014) proposed that the most physically motivated quantity to consider to explore the presence of secondary dependences in the MZR is the offset of the sSFR from that expected, at a given stellar mass, for a typical galaxy lying on the star-forming main sequence (SFMS, Noeske et al. 2007). In this way the implicit mass selection introduced when considering the (s)SFR as the secondary parameter driving the scatter of the MZR can be removed. For the purposes of this analysis we have binned our data in bins of 0.15 dex in $M_\star$ to analyse the dependence of Δlog(O/H) (i.e. the residuals around our best-fitting MZR) on Δlog(sSFR), the latter quantity being defined as:

$$\Delta \log(\text{sSFR}) = \log(\text{sSFR}) - \langle \log(\text{sSFR}) \rangle_{M_\star} \quad (4)$$

where the last term is the expected sSFR at a given $M_\star$, assumed as the median sSFR within 0.15 dex mass bins in our case. The choice of such bin sizes allows us to study these trends minimizing the internal effects of the involved relationships (i.e. doing the analysis 'at fixed stellar mass') while keeping a statistically meaningful number of galaxies inside each bin. The choice of narrower bin sizes does not qualitatively change the inferred results, while larger bin sizes in $M_\star$ (or, in the worse case, not binning at all) can wash out the dependence of metallicity on SFR, due to its differential tightness in different mass regimes (e.g. Sánchez et al. 2017; Barrera-Ballesteros et al. 2017; Sánchez et al. 2019; see also Cresci et al. 2018 for an in-depth discussion of the problem). Nothing changes in our analysis even if we consider the total metallicities (instead of the MZR residuals), thus completely removing any possible parametrization (which means that the internal effect of the MZR in our bins is almost negligible).

In Fig. 8 we plot the metallicity of individual galaxies within each bin as a function of Δlog(sSFR). We are here considering only $M_\star$ bins including more than 100 galaxies. The red line represents the running median of our data inside each bin. The Z–Δlog(sSFR) anti-correlation is clear in the low-mass bins over the entire range of sSFR values, becomes relevant only for sSFR above the SFMS for the intermediate-mass bins and disappears at the highest masses. At low masses (log($M_\star$) < 9.5), this dependence can be accounted for with a linear relation across the whole Δlog(sSFR) range, while for increasing $M_\star$ a sharp increase in slope starts to occur

at Δlog(sSFR) > 0, similar to what was shown for the different Z–sSFR curves at fixed stellar mass in the bottom right-hand panel of Fig. 6. In any case, when accounting for this secondary dependence, the dispersion in metallicity for individual galaxies within each $M_\star$ bin is reduced by a factor of 2–5 per cent in the highest-mass bins, up to a factor of ∼15 per cent in the intermediate-mass bins and by almost 30 per cent in the low-mass bins, as highlighted by the σ and σ_{corr} values reported within each panel of Fig. 8.

4.2 The dependence of the MZR parameters on SFR

To investigate in more detail the nature of the dependence of the MZR on SFR and assess the variations in its parameters, we perform a fit for all the different SFR-dependent mass–metallicity relations, assuming the same functional form presented in equation (2). In the following analysis we primarily refer to SFR as the total SFR (unless stated otherwise). Moreover, we here consider only those subsamples in SFR that allow us to robustly constrain all the MZR parameters, probing in particular both the turnover mass and the low-mass-end regimes. For this reason we limit the analysis to those MZR curves sampled by at least 10 points (i.e $M_\star$–SFR bins); each of those contains at least 25 galaxies.

A first run of the fit demonstrates that the saturation metallicity Z_0 remains constant over the entire range of SFR considered, with very small variations (of the order of ∼0.01 dex) residing well within the typical uncertainties on metallicity measurements. This suggests that the asymptotic limit of chemical enrichment in galaxies, which is regulated by the effective yield of metal production, modulo the impact of outflows, does not depend on the SFR. Therefore, the majority of the SFR dependence of the MZR is accounted for in the variations of the slope and the turnover mass. We then make a second run of the fit, this time fixing the Z_0 value to those derived for the global MZR, while leaving the other parameters free to vary. Although the trend in the β parameter with SFR in the first run is almost constant, we decide to leave this parameter unconstrained to allow the various curves to adjust the shape of the knee and better catch the true values of M_0 and γ. Forcing β to a fixed value would introduce noise, especially in the γ-versus-SFR trend, since β and γ are largely covariant. The uncertainties on the parameters of the different SFR-dependent MZRs are estimated from the 1σ
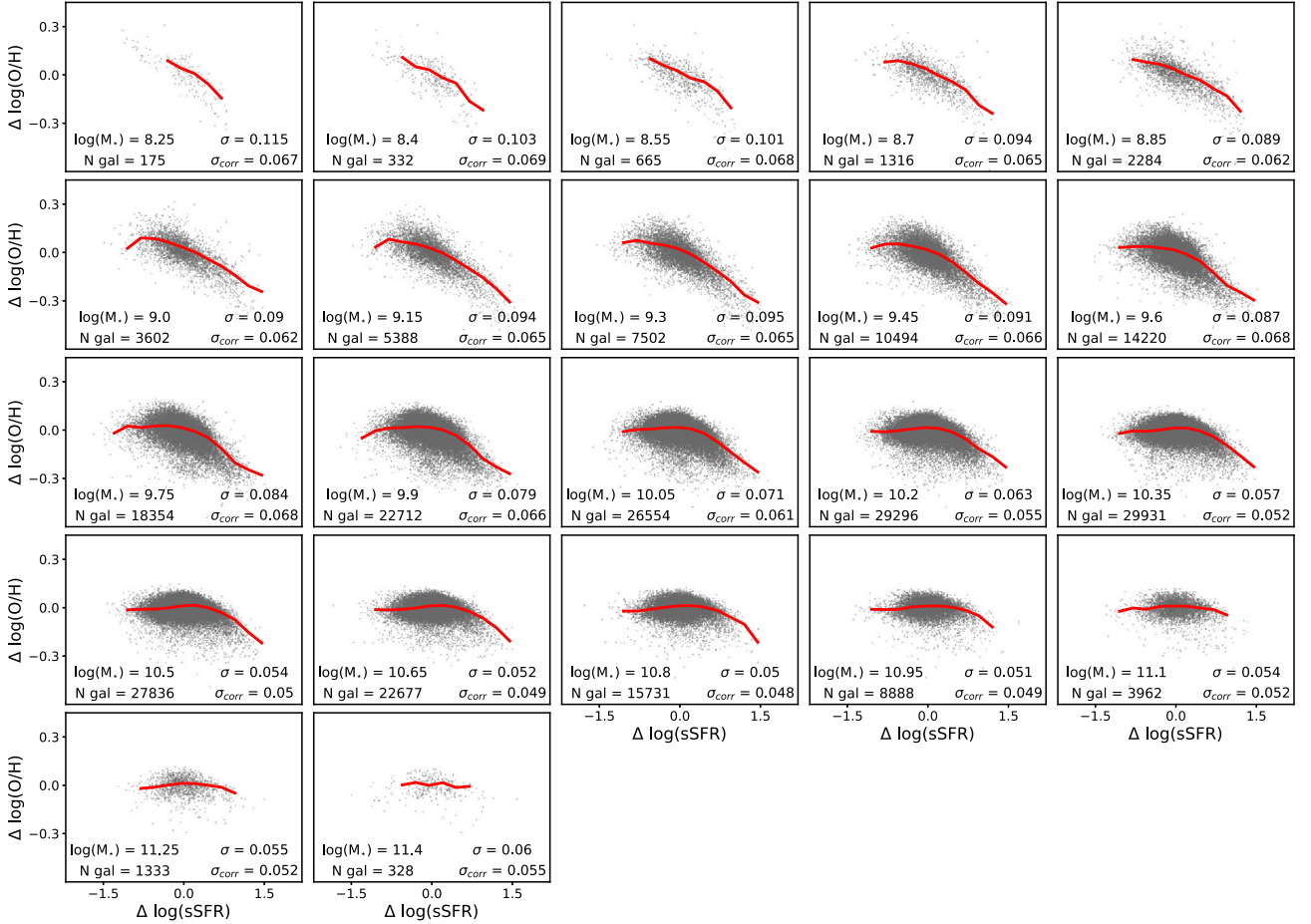
Figure 8. Metallicity residuals around the MZR as a function of $\Delta\log(\text{sSFR})$, i.e. the offset from the star-forming main sequence, for different 0.15 dex wide stellar mass bins. Red lines in each panel are running medians in bins of $\Delta\log(\text{sSFR})$. The number of galaxies per bin is indicated in the bottom left-hand corner of each panel, while in the bottom right-hand corner are reported both the metallicity dispersion of individual galaxies inside the mass bin (σ) and the dispersion after correcting for the secondary dependence on $\Delta\log(\text{sSFR})$ (σ_{corr}). Accounting for this secondary dependence decreases the metallicity dispersion in all $M_\star$ bins, especially at low and intermediate masses (allowing for a reduction in the scatter by a factor up to $\sim$30 per cent).

confidence intervals calculated in our fitting procedure. The results are shown in the upper panel of Fig. 9 and the best-fitting parameters are reported in Table 5. In the lower panels of Fig. 9 we show how the MZR parameters behave with varying SFR: M_0 increases almost linearly with SFR while, in contrast, γ remains almost constant up to $\log(\text{SFR}) = 0.75$ and then shows a rise upward in the last SFR bins where, however, the uncertainties are much larger due to the poorer sampling of the low-mass end of the MZR for such SFR subsamples.

An increase in the slope γ with SFR would mean that the relationship between Z and $M_\star$ is steeper, especially at low masses, for different star-forming populations. On one hand, this could be explained as a manifestation of the chemical downsizing scenario: high-mass–high-SFR galaxies have already converted a large amount of their gas in stars, faster than low-mass–high-SFR galaxies, which are characterized by larger residual gas fractions. Therefore, the higher the SFR considered, the more chemically evolved high-mass galaxies are compared to low-mass ones. On the other hand, this trend can also be ascribed to the differential impact of gas flows: dilution effects may be prominent in low-mass–high-SFR galaxies experiencing large inflows of metal-poor gas, while outflows (which might eject metal-enriched gas) are expected to be much more effective in small galaxies than in high-mass ones, with

a relative importance that correlates with the current level of star formation.

The observed trend in the slope is robust against the choice of different metallicity diagnostics, and is clearly also present when adopting the modified version of the Zahid et al. (2014b) parametrization of the MZR. Nevertheless, the amplitude of the variation of γ with increasing SFR can change when considering metallicity calculated without involving the R_3 and R_2 indicators (or a combination of them; see also Appendix B). In fact, we have tested that, on average, the metallicities of individual galaxies in the high-mass ($\log(M_\star) > 10$)–high-SFR ($\log(\text{SFR}) \gtrsim 0$) regime calculated including the above-mentioned line ratios are systematically lower (by $\sim$0.025 dex) than those calculated by using N_2 only: this causes the median metallicity of our bins in that region to be lower, causing a steepening of the slope. In contrast, the metallicity in the low-SFR regime is higher on average when computed from R_3 and R_2, inducing flatter slopes and thus increasing the amplitude of the variation of γ with SFR. This effect may be introduced by the intrinsic dependence of R_3 on the ionization parameter, which is also related to the average level of star formation within a galaxy. Moreover, as previously stated, the behaviour of the γ parameter is less robustly constrained, given the non-optimal sampling of the low-mass–high-SFR regime and the high covariance of β and γ.
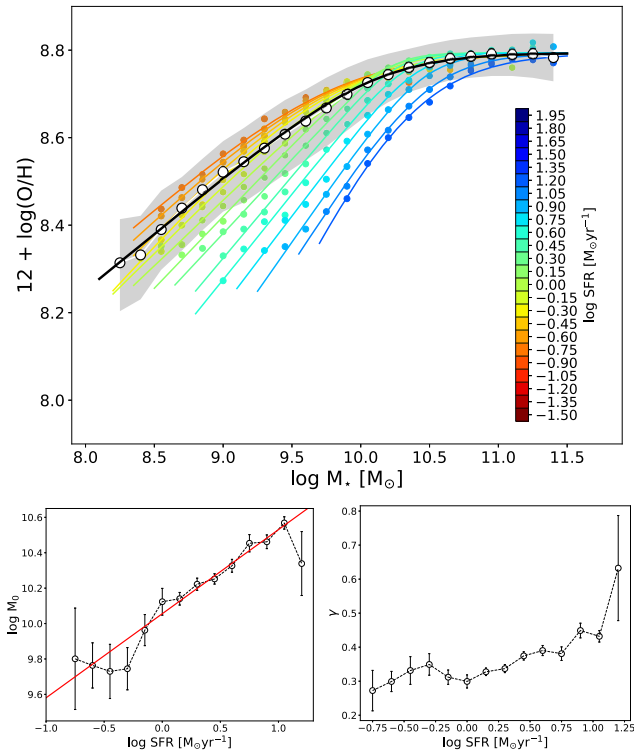
Figure 9. *Upper panel:* Mass–metallicity relations for different values of total SFR. Coloured circles are median metallicities in bins of $\log(M_\star)$ and $\log(\text{SFR})$ (colour-coded by SFR), while thick coloured lines are the various MZR fits for different SFR values, assuming the same MZR parametrization as in equation (2). The white points (grey area) represent the median metallicity (1σ dispersion) in each stellar mass bin and the black curve is the global MZR fit as already shown in Figs 3 and 6. *Bottom panels:* Variation of the parameters of the mass–metallicity relation according to equation (2) as a function of SFR, as a result of the fitted curves presented in the above panel. The saturation metallicity Z_0 is fixed in the fit to its global value, while the width of the knee β is left free to vary but does not show any clear dependence on SFR. The turnover mass M_0 show a clear dependence on the star-formation rate, which can be accounted for with a linear fit to the points (as shown by the red curve). The low-mass-end slope γ, instead, only slightly increases in correspondence with the highest SFR bins.

Therefore, we conclude that the γ-versus-SFR trend shown in Fig. 9 could be driven by physical effects, although selection effects and the use of different metallicity diagnostics might modify the nature of the observed dependence. The variation of M_0 with SFR is instead much more evident and robust against the various issues discussed above. Its possible physical interpretation is related to variations in the gas-to-stellar mass ratio (Zahid et al. 2014a): local high-SFR galaxies (in a way similar to the average galaxy populations at higher redshifts) are characterized by larger gas masses for a given $M_\star$; thus the turnover in the MZR for such populations occurs at higher stellar masses.

4.3 A new parametrization for the FMR

The mutual dependences between $M_\star$, SFR and metallicity can be easily visualized in the three-dimensional space defined by the same quantities. Mannucci et al. (2010) first observed that galaxies in the local Universe are distributed on a surface in this 3D space, the fundamental metallicity relation (FMR), which is affected by a dispersion in metallicity of the order of the uncertainties associated

Table 5. Best-fitting parameters for the different MZR at fixed SFR showed in Fig. 9, according to the MZR parametrization of equation (2). Z_0 has been fixed in the fitting procedure to its global MZR value.

$\log(\text{SFR})$	Z_0	$\log(M_0/\text{M}_\odot)$	γ	β
-0.75	8.79	9.81 ± 0.29	0.27 ± 0.06	1.0 ± 0.1
-0.6	8.79	9.77 ± 0.13	0.30 ± 0.03	1.0 ± 0.1
-0.45	8.79	9.74 ± 0.15	0.33 ± 0.04	1.0 ± 0.1
-0.3	8.79	9.75 ± 0.12	0.35 ± 0.03	1.0 ± 0.1
-0.15	8.79	9.96 ± 0.09	0.31 ± 0.02	1.3 ± 0.2
-0.0	8.79	10.12 ± 0.08	0.30 ± 0.02	1.9 ± 0.5
0.15	8.79	10.14 ± 0.04	0.33 ± 0.01	2.3 ± 0.4
0.3	8.79	10.22 ± 0.03	0.34 ± 0.01	3.2 ± 0.9
0.45	8.79	10.25 ± 0.03	0.38 ± 0.01	3.1 ± 0.6
0.6	8.79	10.33 ± 0.04	0.39 ± 0.02	2.9 ± 0.7
0.75	8.79	10.40 ± 0.05	0.41 ± 0.02	2.7 ± 0.6
0.9	8.79	10.46 ± 0.04	0.45 ± 0.02	2.4 ± 0.4
1.05	8.79	10.48 ± 0.06	0.49 ± 0.04	1.7 ± 0.2
1.2	8.79	10.33 ± 0.19	0.64 ± 0.16	1.3 ± 0.2

with the measurement processes. This surface is clearly revealed by the distribution of the median-binned values of $M_\star$, SFR and $\log(\text{O/H})$ in the reference 3D space (upper panel of Fig. A1); points are colour-coded by the number of galaxies in each bin, to allow for a better visualization of how the surface is populated by galaxies in the local Universe. The existence of such a surface means that, on average, the metallicity properties of galaxies can be predicted once their $M_\star$ and SFR are known.

Mannucci et al. (2010) originally parametrized the FMR with a second-grade polynomial surface. However, we have shown in Section 4.2 that most of the secondary dependence of the MZR can be accounted for by the variation of the turnover mass (M_0), while the small trend seen in the low-mass-end slope γ, although present, can be almost neglected up to the highest SFR considered. Therefore, we propose a new functional form to analytically describe the FMR, by explicitly introducing the SFR dependence of the turnover mass M_0 into equation (2) by allowing it to vary linearly with SFR. This new parametrization would be better suited than the simple second-order polynomial surface to account for the saturation metallicity limit at high masses and the trends in M_0 with SFR. We decide here not to include any explicit dependence of the slope γ on SFR, because even a linear trend may produce risky extrapolations in the low-mass–high-SFR regime, which is poorly sampled and thus poorly constrained by SDSS galaxies, but it is largely populated by high-redshift sources. This is equivalent to assuming that the dependence of the MZR on SFR can be fully accounted for by the variation of M_0; to better visualize the consequences of this assumption, we refer the reader to the analysis presented in Appendix A.

Our newly proposed functional form for the FMR is thus the following:

$$Z(M, \text{SFR}) = Z_0 - \gamma/\beta \log(1 + (M/M_0(\text{SFR}))^{-\beta}) \quad (5)$$

where $\log(M_0(\text{SFR})) = m_0 + m_1 \log(\text{SFR})$ or, equivalently, $M_0(\text{SFR}) = \Theta_0 \cdot \text{SFR}^{m_1}$, where $\Theta_0 = 10^{m_0}$.

The best-fitting parameters obtained by fitting this equation to our median-binned data are reported in Table 6 and the shape of the newly parametrized surface in the M–Z–SFR space is shown in the upper panel of Fig. 10 by the black grid. The scatter of median values around the best-fitting analytical representation of the FMR is remarkably small ($\sigma_M = 0.028$ dex), with the dispersion in metallicity of individual galaxies decreasing instead to $\sigma_{\text{FMR}} = 0.054$ dex from $\sigma_{\text{MZR}} = 0.07$, a reduction of $\sim$23 per cent. The residual

Table 6. Best-fitting parameters for the FMR parametrization of equation (5), assuming both total and fibre SFR.

	Z_0	m_0	m_1	γ	β
Total SFR	8.779 ± 0.005	10.11 ± 0.03	0.56 ± 0.01	0.31 ± 0.01	2.1 ± 0.4
Fibre SFR	8.782 ± 0.004	10.39 ± 0.03	0.454 ± 0.008	0.299 ± 0.008	2.6 ± 0.5

scatter of individual objects around the FMR is comparable with the typical uncertainties associated with the metallicity determination via the strong-line method and can probably not be reduced further at this stage. However, it should also be stressed here that, when considering the population as a whole, a large contribution to the residual scatter comes from high-mass galaxies where the effects of the FMR are less relevant; indeed, we have already shown in Section 4.1 that a more significant reduction of the dispersion (up to 30 per cent) is obtained when considering the role of SFR at fixed stellar mass (and in particular at low $M_\star$) following a non-parametric approach.

In the bottom panel of Fig. 10, the FMR is graphically represented by a continuous surface, colour-coded by its predicted metallicity. On the $M_\star$–Z and SFR–Z planes, we show the contours of the relative 2D projections of the FMR, nicely reproducing the mutual dependences between metallicity and SFR (at fixed $M_\star$) and between metallicity and stellar mass (at fixed SFR) observed in our sample and shown in Fig. 6.

The same analysis described above on the FMR has also been performed assuming fibre SFR rather than total SFR. Comparing the two representations of the FMR, the metallicity predicted is identical in the flat saturation region at high mass and low SFR while, on average, the 'fibre-based' FMR predicts lower metallicities (of the order of 0.05 dex) than the 'total-SFR' FMR as we move towards the low-mass–high-SFR region. This is the direct natural consequence of assigning a galaxy with fixed $M_\star$ and metallicity to a higher SFR bin when applying the aperture corrections. For completeness, and to allow a proper comparison of the predictions of the FMR presented in this paper with the largest possible variety of data (i.e. from fibre and/or IFU spectroscopy, on local and high-z galaxies), we therefore provide also the best-fitting parameters of the FMR based on SFR measurements inside the fibre: these are reported in Table 6.

The metallicity predictions provided by the FMR of equation (5) span a wider region of the $M_\star$, SFR parameter space than that covered by the calibration sample of local SDSS galaxies. Indeed, the FMR is often used to predict the metallicity outside the ranges of mass and SFR where it is defined, especially in high-redshift studies, where galaxies are characterized, on average, by higher SFRs compared to local ones. This means that, when comparing metallicities observed in high-z sources, even when rescaled to the proper T_e abundance scale, one is often forced to rely on extrapolations of the locally calibrated FMR, mainly in the high-SFR regime, and this effect should be carefully taken into account when trying to assess and interpret the evolution of the FMR with redshift.

In order to give an estimate of the uncertainties associated with the extrapolations of the FMR represented by equation (5) (implicitly assuming the validity of the underlying physical background), we run an MCMC by letting the different FMR parameters randomly vary within their uncertainties following a normal distribution. We thus generate 1000 different realizations of the FMR and compute the dispersion in the metallicity predictions at each fixed

value on an $M_\star$ and SFR grid. The results of this test are shown in Fig. 11. For comparison, the $M_\star$–(total) SFR binning scheme adopted in this work, which defines the region of the parameter space covered by local galaxies, is superimposed in black. Higher uncertainties (of the order of $\gtrsim$0.3 dex) are found to occur in the low-mass–high-SFR regime (the region of the FMR with the lowest predicted metallicity); this is not surprising, as it is mainly driven by the uncertainties on the low-mass-end slope. We also note that this represents the region of most extreme extrapolation, where we do not have any constraint from the observed data. We stress here that Fig. 11 gives only a rough estimate of the typical uncertainty associated with the hereby presented analytical form of the FMR. Neither the potential uncertainties related to measurement errors of the involved quantities, nor those arising from the choice of a different parametrization, are considered at this stage. However, every observational study aiming at comparing measured metallicities with extrapolation of the FMR provided in this work should consider this minimum level of uncertainty in the interpretation of the results.

5 SUMMARY AND CONCLUSIONS

We have analysed the scaling relations between stellar mass, metallicity and star-formation rate in the local Universe in light of the metallicity calibrations introduced by Curti et al. (2017), and complemented in this work, which are fully based on the T_e abundance scale defined for SDSS galaxies (Fig. 1). The main conclusions reached in this paper can be summarized as follows.

(i) We have parametrized the mass–metallicity relation with a new functional form (equation 2 and upper panel of Fig. 3), which allows us to control the width of the knee (β) and better capture the value of the turnover mass (M_0), which we find to occur at $\log(M_\star/M_\odot) = 10.02 \pm 0.09$. The low-mass-end slope of our MZR is $\gamma = 0.28 \pm 0.02$ and approaches saturation metallicity at $Z_0 = 8.793 \pm 0.005$ (i.e. about 1.27 times $Z_\odot$). The dispersion in metallicity of individual galaxies around the median relation is 0.07 dex.

(ii) A comparison between our new MZR and previous assessments in the literature is shown in the bottom panel of Fig. 3. Our MZR deviates from those based on abundances predicted by grids of photoionization models, in the sense of a lower normalization of the high-mass regime of ∼0.3 dex, while showing good consistency with different determinations of the relation based on T_e metallicities. The agreement with Andrews & Martini (2013) in particular is remarkable, despite a small divergence in the low-mass regime. The MZR by Yates et al. (2019) presents a systematic offset towards lower abundances at fixed stellar mass, possibly due to selection effects driven by the requirement of a [O III]λ4363 detection, or by the different average SFR (and size) of the studied sample. Our strong-line MZR is also consistent with the independent measurements of chemical abundances obtained by means of spectroscopy of blue and red supergiants in very nearby galaxies
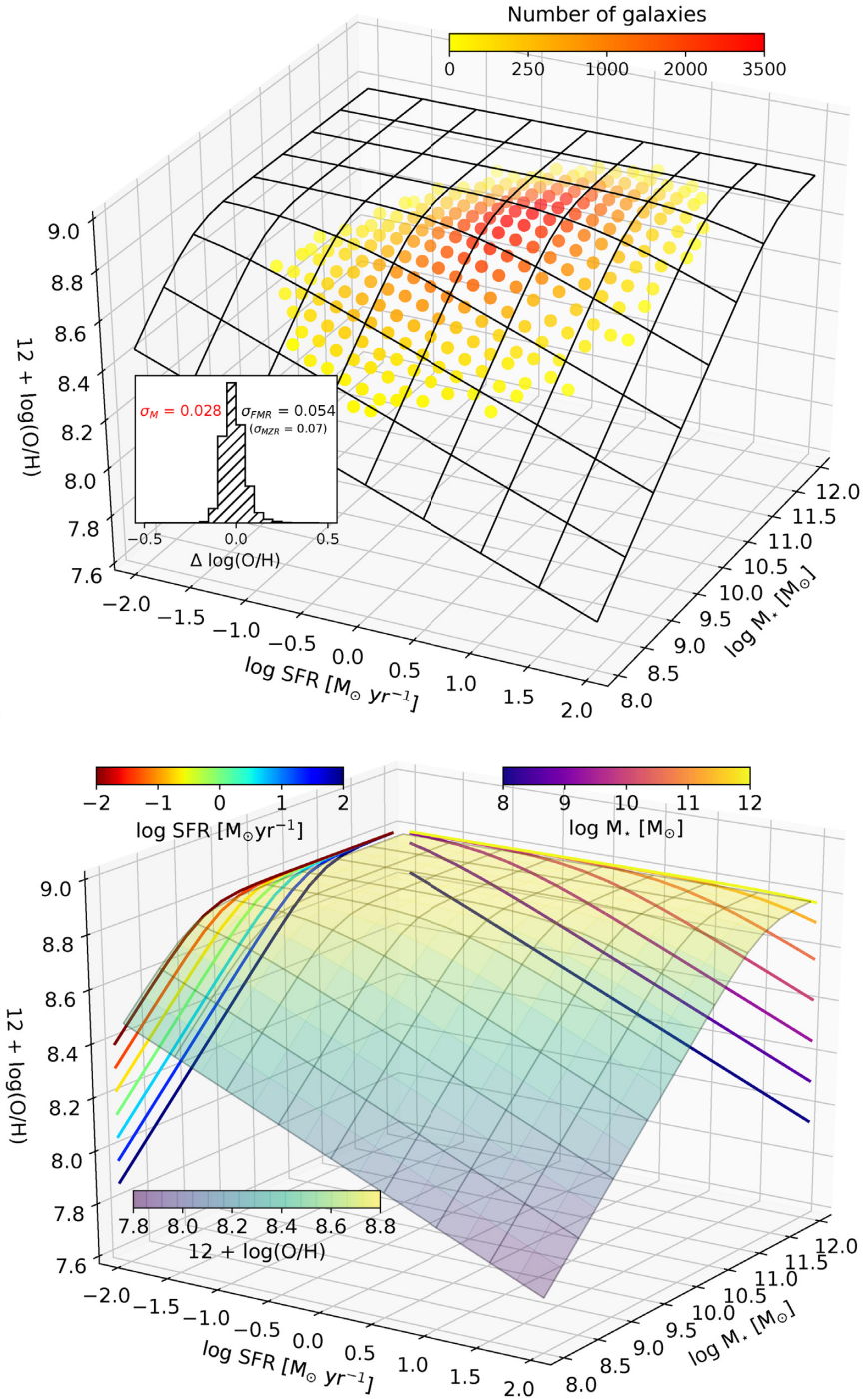
Figure 10. *Upper panel*: 3D visualization of the mass–metallicity–SFR relation for our $M_\star$–SFR bins as described in Section 4, colour-coded by the number of galaxies in each bin. A sampling of the best-fitting surface representing the FMR from equation (5) is shown by the black grid, while the histogram of metallicity dispersion of individual galaxies around the surface is reported in the small box. The three quoted σ values represent respectively the dispersion of the median-binned values around the surface (σ_M, in red), the scatter of individual galaxies around the surface ($\sigma_{\rm FMR}$), and, for comparison, the scatter of individual galaxies around the best-fitting MZR ($\sigma_{\rm MZR}$). *Bottom panel*: Graphical representation of the FMR surface, colour-coded by its predicted metallicity values. The contours of the projections of the FMR on to the $M_\star$–Z and SFR–Z planes are also drawn, nicely reproducing the observed trends shown in Fig. 6.

(Davies et al. 2017) at high masses, while slightly deviating from the median relation below $\log(M_\star) < 9.5$, nevertheless confirming the good agreement between the T_e scale for abundances of the ISM and that defined by stellar abundances as measured in young massive stars.

(iii) The MZR shows a clear dependence on star-formation rate, both considering total SFR or SFR within the fibre, which is more evident in low $M_\star$–high SFR regimes (Fig. 6, left). The dependence of metallicity on SFR, at fixed stellar mass, can also be visualized by plotting $\log(O/H)$ against (s)SFR for median-binned
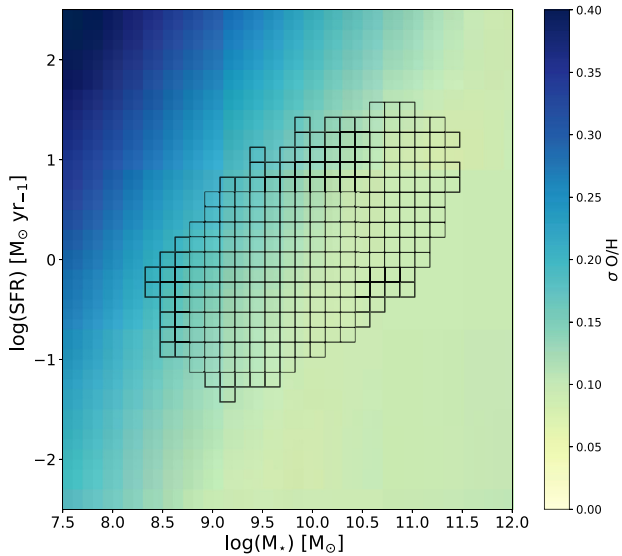
Figure 11. Minimum uncertainties associated with the metallicity predictions provided by the FMR parametrization of equation (5), as computed from 1000 different realizations obtained varying the FMR parameters in an MCMC simulation. The $M_\star$–SFR binning grid defined in this work by local SDSS galaxies is superimposed in black. The higher level of uncertainty ($\gtrsim 0.3$ dex) is obtained in the low-mass–high-SFR regime, outside the region covered by the local sample. These values are propagated from the errors on the best-fitting parameters of the FMR and do not take into account other sources of uncertainty, like those associated with the measurements of involved quantities and those simply related to extrapolating a given functional form outside the regime covered by the data.

values (Fig. 6, right) or the MZR residuals versus ΔsSFR (i.e. the distance from the SFMS) for individual galaxies in narrow mass bins (Fig. 8, as originally suggested by Salim et al. 2014). The anti-correlation between metallicity and SFR appears strong at low masses, decreasing for increasing $M_\star$ until disappearing at high masses. When accounting for the Z–SFR dependence, the scatter in each individual mass bin is reduced, for individual galaxies, by a factor of $\sim$15 per cent at intermediate masses and up to a factor of $\sim$30 per cent in some of the lowest-mass bins. However, intense star-forming galaxies (log(sSFR) $\lesssim -9.5$) maintain the dependence between log(O/H) and (s)SFR at almost all masses.

(iv) We have parametrized the M–Z–SFR relation with the same functional form adopted for the MZR, investigating the dependence of its main parameters on SFR (Fig. 9). The turnover mass M_0 shows a clear trend with varying SFR, while the saturation metallicity does not change. The turnover mass increases with SFR, as a possible consequence of the different gas-to-star mass ratio in highly star-forming galaxies (as also suggested by Zahid et al. 2014b). The variation of the slope γ with SFR is much shallower and may be affected by how different populations of galaxies react to the effects of outflows; however, this latter quantity is also sensitive to the choice of the metallicity diagnostics and to selection effects.

(v) The scatter of galaxy population is reduced when considering a relation in the three-dimensional space defined by $M_\star$, metallicity and SFR, the so-called fundamental metallicity relation (FMR). We explicitly introduced the dependence of M_0 on SFR to derive a new functional form of the FMR (equation 5 and Fig. 10). The scatter around this new relation is only 0.028 dex for median values in bins of $M_\star$ and SFR and 0.054 for the global population of individual galaxies, a reduction of $\sim$22 per cent compared to the scatter around

the MZR only. However, we note that a large contribution to the residual global scatter comes from highly populated high-$M_\star$ bins, where the effects of the FMR are less relevant.

(vi) The new parametrization of the FMR provided here represents a local benchmark to be compared with chemical evolution models and observations (of both local and high-redshift galaxies), which are tied to the T_e abundance scale. An estimate of the (minimum) uncertainties associated with the metallicity predictions of the new FMR is presented in Fig. 11: the uncertainties increase up to $\sim$0.3 dex in the low-mass–high-SFR regime, outside the region sampled by local galaxies.

REFERENCES

Abazajian K. N. et al., 2009, ApJS, 182, 543
Allende Prieto C., Lambert D. L., Asplund M., 2001, ApJ, 556, L63
Andrews B. H., Martini P., 2013, ApJ, 765, 140
Barrera-Ballesteros J. K. et al., 2016, MNRAS, 463, 2513
Barrera-Ballesteros J. K., Sánchez S. F., Heckman T., Blanc G. A., The MaNGA Team, 2017, ApJ, 844, 80
Belfiore F. et al., 2017, MNRAS, 469, 151
Bothwell M. S., Maiolino R., Kennicutt R., Cresci G., Mannucci F., Marconi A., Cicone C., 2013, MNRAS, 433, 1425
Bothwell M. S., Maiolino R., Peng Y., Cicone C., Griffith H., Wagg J., 2016a, MNRAS, 455, 1156
Bothwell M. S., Maiolino R., Cicone C., Peng Y., Wagg J., 2016b, A&A, 595, A48
Bresolin F., Kudritzki R.-P., Urbaneja M. A., Gieren W., Ho I.-T., Pietrzyński G., 2016, ApJ, 830, 64
Brinchmann J., Charlot S., White S. D. M., Tremonti C., Kauffmann G., Heckman T., Brinkmann J., 2004, MNRAS, 351, 1151
Cardelli J. A., Clayton G. C., Mathis J. S., 1989, ApJ, 345, 245
Chabrier G., 2003, PASP, 115, 763
Chisholm J., Tremonti C. A., Leitherer C., Chen Y., Wofford A., Lundgren B., 2015, ApJ, 811, 149
Chisholm J., Tremonti C., Leitherer C., 2018, MNRAS, 481, 1690
Cresci G., Mannucci F., Curti M., 2019, A&A, 627, A42
Curti M., Cresci G., Mannucci F., Marconi A., Maiolino R., Esposito S., 2017, MNRAS, 465, 1384
Davé R., Finlator K., Oppenheimer B. D., 2011, MNRAS, 416, 1354
Davé R., Rafieferantsoa M. H., Thompson R. J., Hopkins P. F., 2017, MNRAS, 467, 115
Davies B., Kudritzki R.-P., Gazak Z., Plez B., Bergemann M., Evans C., Patrick L., 2015, ApJ, 806, 21

Davies B. et al., 2017, ApJ, 847, 112

Dayal P., Ferrara A., Dunlop J. S., 2013, MNRAS, 430, 2891

De Rossi M. E., Theuns T., Font A. S., McCarthy I. G., 2015, MNRAS, 452, 486

De Rossi M. E., Bower R. G., Font A. S., Schaye J., Theuns T., 2017, MNRAS, 472, 3354

Ellison S. L., Patton D. R., Simard L., McConnachie A. W., 2008, ApJ, 672, L107

Erb D. K., Shapley A. E., Pettini M., Steidel C. C., Reddy N. A., Adelberger K. L., 2006a, ApJ, 644, 813

Erb D. K., Steidel C. C., Shapley A. E., Pettini M., Reddy N. A., Adelberger K. L., 2006b, ApJ, 646, 107

Gao Y. et al., 2018, ApJ, 868, 2, 89

Gazak J. Z. et al., 2015, ApJ, 805, 182

Grasshorn Gebhardt H. S., Zeimann G. R., Ciardullo R., Gronwall C., Hagen A., Bridge J. S., Schneider D. P., Trump J. R., 2016, ApJ, 817, 10

Hirschauer A. S., Salzer J. J., Janowiecki S., Wegner G. A., 2018, AJ, 155, 82

Hunt L., Dayal P., Magrini L., Ferrara A., 2016, MNRAS, 463, 2002

Kashino D., Renzini A., Silverman J. D., Daddi E., 2016, ApJ, 823, L24

Kauffmann G. et al., 2003a, MNRAS, 341, 33

Kauffmann G. et al., 2003b, MNRAS, 346, 1055

Kennicutt R. C., Evans N. J., 2012, ARA&A, 50, 531

Kewley L. J., Dopita M. A., 2002, ApJS, 142, 35

Kewley L. J., Ellison S. L., 2008, ApJ, 681, 1183

Kobulnicky H. A., Kewley L. J., 2004, ApJ, 617, 240

Kudritzki R. P., Castro N., Urbaneja M. A., Ho I.-T., Bresolin F., Gieren W., Pietrzyński G., Przybilla N., 2016, ApJ, 829, 70

Lagos C. d. P. et al., 2016, MNRAS, 459, 2632

Lequeux J., Peimbert M., Rayo J. F., Serrano A., Torres-Peimbert S., 1979, A&A, 80, 155

Lian J., Thomas D., Maraston C., 2018, MNRAS, 481, 4000

Lilly S. J., Carollo C. M., Pipino A., Renzini A., Peng Y., 2013, ApJ, 772, 119

López-Sánchez Á. R., Dopita M. A., Kewley L. J., Zahid H. J., Nicholls D. C., Scharwächter J., 2012, MNRAS, 426, 2630

Ly C., Malkan M. A., Rigby J. R., Nagao T., 2016, ApJ, 828, 67

Maiolino R., Mannucci F., 2019, A&AR, 27, 3

Maiolino R. et al., 2008, A&A, 488, 463

Mannucci F. et al., 2009, MNRAS, 398, 1915

Mannucci F., Cresci G., Maiolino R., Marconi A., Gnerucci A., 2010, MNRAS, 408, 2115

Mannucci F., Salvaterra R., Campisi M. A., 2011, MNRAS, 414, 1263

Moustakas J. et al., 2011, preprint (arXiv:1112.3300)

Nakajima K., Ouchi M., 2014, MNRAS, 442, 900

Newville M., Stensitzki T., Allen D. B., Ingargiola A., 2014, LMFIT: Non-Linear Least-Square Minimization and Curve-Fitting for Python, Zenodo

Noeske K. G. et al., 2007, ApJ, 660, L47

Peimbert M., 1967, ApJ, 150, 825

Pettini M., Pagel B. E. J., 2004, MNRAS, 348, L59

Planck Collaboration et al., 2016, A&A, 594, A13

Richards S. N. et al., 2016, MNRAS, 455, 2826

Salim S. et al., 2007, ApJS, 173, 267

Salim S., Lee J. C., Ly C., Brinchmann J., Davé R., Dickinson M., Salzer J. J., Charlot S., 2014, ApJ, 797, 126

Sánchez Almeida J., Caon N., Muñoz-Tuñón C.,Filho M., Cerviño M. , 2018, MNRAS, 476, 4765

Sánchez-Menguiano L., Sánchez Almeida J., Muñoz-Tuñón C., Sánchez S. F., Filho M., Hwang H.-C., Drory N., 2019, ApJ, 882, 9

Sánchez S. F. et al., 2017, MNRAS, 469, 2121

Sánchez S. F. et al., 2019, MNRAS, 484, 3042

Sanders R. L., Shapley A. E., Zhang K., Yan R., 2017, ApJ, 850, 136

Sanders R. L. et al., 2018, ApJ, 858, 99

Somerville R. S., Davé R., 2015, ARA&A, 53, 51

Stasińska G., 2002, preprint (arXiv:astro-ph/0207500)

Stasińska G., 2005, A&A, 434, 507

Telford O. G., Dalcanton J. J., Skillman E. D., Conroy C., 2016, ApJ, 827, 35

The Astropy Collaboration et al., 2018, ApJ, 156, 123

Torrey P. et al., 2018, MNRAS, 477, L16

Tremonti C. A. et al., 2004, ApJ, 613, 898

Vale Asari N., Couto G. S., Cid Fernandes R., Stasińska G., de Amorim A. L., Ruschel-Dutra D., Werle A., Florido T. Z., 2019, MNRAS, 489, 4721

Yabe K. et al., 2015, PASJ, 67, 102

Yates R. M., Kauffmann G., Guo Q., 2012, MNRAS, 422, 215

Yates R. M., Schady P., Chen T.-W., Schweyer T., Wiseman P., 2019, preprint (arXiv:1901.02890)

York D. G. et al., 2000, AJ, 120, 1579

Zahid H. J., Kewley L. J., Bresolin F., 2011, ApJ, 730, 137

Zahid H. J., Dima G. I., Kudritzki R.-P., Kewley L. J., Geller M. J., Hwang H. S., Silverman J. D., Kashino D., 2014a, ApJ, 791, 130

Zahid H. J. et al., 2014b, ApJ, 792, 75

Zhang K. et al., 2017, MNRAS, 466, 3217

APPENDIX A: THE PROJECTION OF MINIMUM SCATTER

Following Mannucci et al. (2010), we search for the 2D projection of the FMR that reduce the metallicity scatter around the relation Z–μ_α, where $\mu_\alpha = \log(M_\star) - \alpha \log(\text{SFR})$. In this framework, α is the parameter that quantifies the strength of the Z–SFR correlation at fixed stellar mass: for $\alpha = 0$ the relation reduces to the MZR, meaning no correlation between metallicity and SFR, while larger values of α would imply stronger correlation between metallicity and SFR. We fit our M–SFR bins (we here consider total SFR only) against log(O/H) according to the same functional form used for the MZR (i.e. equation 2), where the x-variable is now μ_α: the results are show in Fig. A1 and reported in the first row of Table A1. We obtain a best-fitting α value of 0.55, larger than that found by Mannucci et al. (2010) ($\alpha = 0.32$) but lower than other previous estimates (e.g. $\alpha = 0.66$ as found by Andrews & Martini 2013); however, it is well known that the relative strength of the secondary dependence of the MZR on the SFR can be strongly affected by many factors, primarily related to selection biases and the choice of the metallicity calibrations. Moreover, we have seen in the previous sections how the tightness of the Z–SFR relation changes as a function of the SFR itself; this induce a change in the slope of the different MZRs at fixed SFR, whose effect can be clearly seen in the upper panel of Fig. A1, where the residuals around the best fit still correlate with the SFR as the highest star-forming galaxies (blue points) would require steeper slopes to be reproduced compared to low star-formers (red points). Indeed, to obtain a perfect and linear 2D projection on the Z–μ_α plane would require only a variation in M_0, such that the slopes of the different MZRs at fixed SFR do not intercept when rotating the FMR around the 'log(O/H) axis'. This can also be visualized by plotting the metallicity against $M_\star$ normalized to the turnover mass M_0 for each SFR subsample (similarly to that done by Zahid et al. 2014a for samples at different redshifts), fixing at the same time the slope γ: if the evolution of the MZR with SFR resides entirely in the variation of M_0, such a change of variable should remove the scatter around the new relation (similarly to that achieved by the 2D projection on Z–μ_α). This is shown in the upper right-hand panel of Fig. A1, where we find qualitatively similar behaviour as in the left-hand panel: the majority of the SFR dependence is removed, but a residual effect, related to the variation in the slope γ with the SFR, is still present. The same result is obtained also assuming the modified Zahid et al. (2014a) functional form of the MZR presented in equation (3).

Therefore, the two upper panels of Fig. A1 both show that accounting for the variation in M_0 only is not enough to completely remove the SFR dependence of the MZR (although accounting for
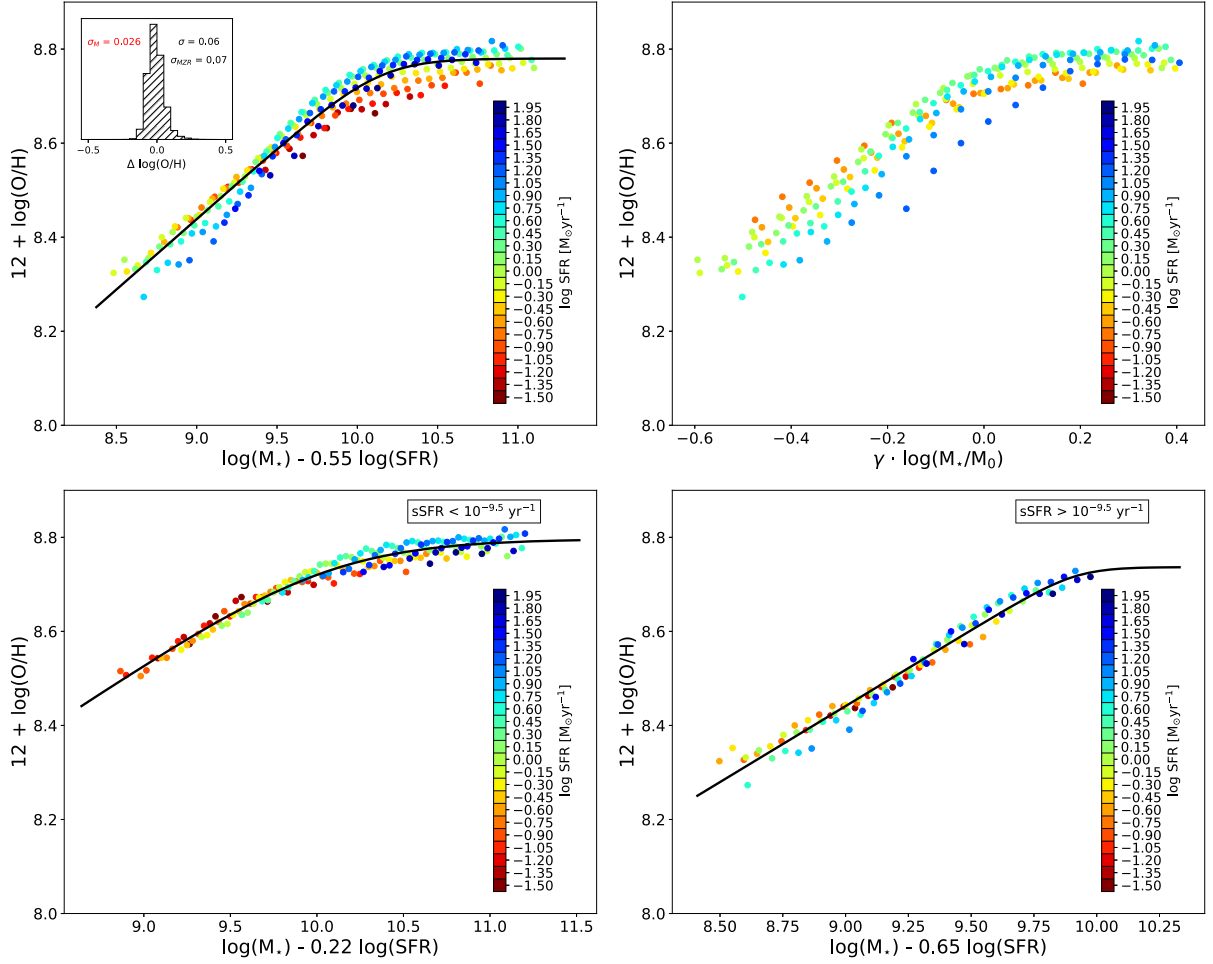
Figure A1. *Upper left*: 2D projection of the *M–Z–SFR* relation on the *Z–μ$_\alpha$* plane, with $\alpha = 0.55$. This projection minimizes the scatter of the median-binned metallicities around the relation defined as $12 + \log(O/H) = \log(M_\star) - \alpha \log(SFR)$. All the points are colour-coded according to their total SFR. In the small box, the histogram of metallicity dispersion of individual galaxies around the surface is reported, together with the dispersion of the median-binned values around the best-fitting relation (σ_M, in red), the scatter of individual galaxies around the best-fitting relation, and the scatter of individual galaxies around the MZR. The variation in the slope for the different SFR regimes is visible, which cannot simply be accounted for by a projection on the *Z–μ$_\alpha$* plane. *Upper right*: Median metallicity plotted against stellar mass normalized to the turnover mass M_0 for each SFR subsample. The residual trend with SFR seen at low masses is indicative of the variation of the slope γ with SFR. *Bottom left*: 2D projection for the 'low-sSFR' subsample (sSFR $< 10^{-9.5}$ [yr^{-1}]). The *Z*–SFR dependence is weaker ($\alpha = 0.22$), but the dispersion around the relation is strongly reduced. *Bottom right*: 2D projection for the 'high-sSFR' subsample (sSFR $> 10^{-9.5}$ [yr^{-1}]). The *Z*–SFR dependence is tighter ($\alpha = 0.65$), but the dispersion is slightly larger compared to the 'low-sSFR' sample.

Table A1. Best-fitting parameters for the 2D projections of the FMR on the *Z–μ$_\alpha$* plane, for different SFR regimes.

	α	Z_0	μ_0	γ	β
Global sample	0.55 ± 0.01	8.780 ± 0.004	10.14 ± 0.03	0.30 ± 0.01	2.4 ± 0.4
sSFR$<10^{-9.5}$ Gyr^{-1}	0.22 ± 0.02	8.796 ± 0.005	10.1 ± 0.1	0.25 ± 0.03	1.1 ± 0.2
sSFR$>10^{-9.5}$ Gyr^{-1}	0.65 ± 0.01	8.74 ± 0.04	9.9 ± 0.1	0.32 ± 0.01	5.0 ± 3.0

its primary source) or, in other words, that the same result cannot be achieved by a simple 2D projection of the FMR, due to the fact that the variation of the strength of the *Z*–SFR correlation with SFR itself is responsible for the change in the slope for the different MZRs at fixed star-formation rate.

However, from what we have seen in Fig. 6, two different regimes can be approximately identified where the shape of the *Z*–SFR relation, at fixed stellar mass, changes substantially,

steepening at all masses for sSFR $\gtrsim 10^{-9.5}$ yr^{-1}. Thus, we can divide our total sample into two subsets of galaxies, the 'high-sSFR' sample ($\log$(sSFR) > -9.5) and the 'low-sSFR' sample ($\log$(sSFR) < -9.5) respectively, bin them in $M_\star$ and SFR and perform the fit again, the results of which are now shown in the bottom panels of Fig. A1 and reported in Table A1. For the low-sSFR sample, the strength of the *Z*–SFR dependence is weaker, as expected ($\alpha = 0.22$); however, the 2D projection now considerably

reduces the scatter of median metallicities for this galaxy population around the new relation for all SFRs. For the high-sSFR sample instead, the *Z*–SFR dependence is now stronger ($\alpha = 0.65$), but the small number of objects populating this regime in the local Universe (only $\sim$15 per cent of the sample analysed in this work) and the largest scatter of these galaxies in each *M*–SFR bin do not allow one to obtain the same level of reduction of the dispersion as for the low-sSFR sample.

## APPENDIX B: SYSTEMATICS OF THE METALLICITY CALIBRATIONS

It is well known that indirect strong-line abundance diagnostics do not always agree with one another when used individually. Although the calibration set presented in Fig. 1 is characterized by a good level of self-consistency (see figs 10 and 11 of Curti et al. 2017), it is impossible to completely remove the underlying discrepancies, given the intrinsically different physical mechanisms responsible for the dependences between the various line ratios considered and the oxygen abundance. Therefore, in order to assess the amplitude of possible systematics in our analysis, here we study the MZR and the *M*–*Z*–SFR relation as obtained adopting only nitrogen-based and only oxygen-based diagnostics. We note here that in this case, on top of the original sample selection described in Section 2, we also had to apply an SNR cut on the [N II]λ6584, [O II]λ3727, 29 and [O III]λ5007 lines in order to perform a meaningful comparison.

In the upper panels of Fig. B1 we show the MZR obtained adopting only a combination of the R_2 and R_3 diagnostics on the left, whereas the MZR based only on the N_2 diagnostic is shown on the right. In both panels, the 'original' MZR derived by combining all the diagnostics together is also shown in blue for reference. In the central panels of the same figure, the *M*–*Z*–SFR relation (as in Fig. 6) in shown in the two different cases as well. It can be seen that the N_2 calibration provides lower abundances (on average) than the combination of R_2 and R_3. This translates into a slightly lower normalization of the MZR, which produces in particular a lower asymptotic metallicity and a steepening of the slope at the low-mass end. Moreover, the strength of the *Z*–SFR relation at fixed stellar mass is increased when considering the $R_2 + R_3$ metallicity, especially in the high-mass–high-SFR regime, as a possible consequence of the different impact that the ionization parameter has on the different abundance diagnostics, in particular R_3 (see also the discussion in Section 4.2).

Overall, these effects are of the order of $\sim$0.025–0.03 dex and appear more prominent when considering the N_2 diagnostic alone. None the less, they do not prevent the detection of the secondary *Z*–SFR dependence, which is clearly visible in both representations. This can also be clearly seen in the bottom panels of Fig. B1 where we plot, as a function of stellar mass, the difference between the median metallicity in bins of $M_\star$ (white points) and bins of $M_\star$–SFR (coloured points) computed with the two different combinations of diagnostics (i.e. [R_2,R_3] and N_2) and the 'original' metallicity adopted throughout the paper (inferred involving all the diagnostics simultaneously). However, we note that for $M_\star$ lower than 10^9 M$_\odot$ and for $M_\star > 10^{10}$ M$_\odot$ and log(SFR) $\gtrsim 1$ the two predictions can diverge up to $\sim$0.05 dex, modifying, as we have seen, the shape of the low-mass end of the MZR and/or the amplitude of the secondary *Z*–SFR dependence. Therefore, we stress the importance that the simultaneous combination of multiple emission line diagnostics has in minimizing these potential systematic effects.
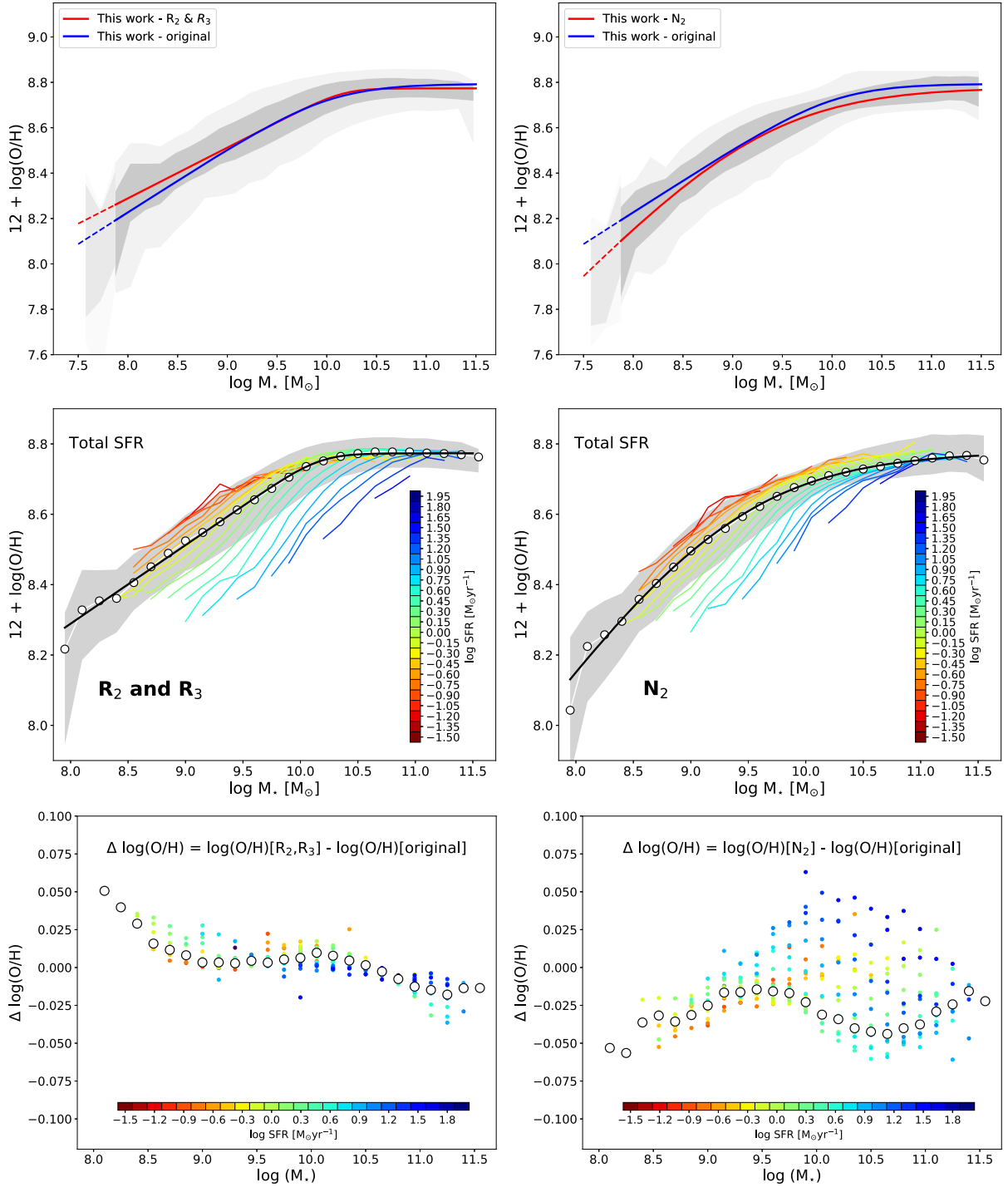
Figure B1. Mass–metallicity and *M–Z*–SFR relations derived adopting only oxygen-based (i.e. R₂ and R₃, left) or nitrogen-based (i.e. N₂, right) diagnostics. In the top panels, the 'original' MZR considered throughout the paper is shown for reference in blue. In the bottom panels we plot, as a function of stellar mass, the difference between the metallicity in bins of stellar mass (white points) and bins of $M_\star$–SFR (coloured points) computed with the relative combination of diagnostics and the 'original' metallicity adopted throughout the paper (i.e. inferred involving all the diagnostics simultaneously). Symbols and colours are the same as in Figs 3 and 6.

This paper has been typeset from a TEX/LATEX file prepared by the author.